Investigating the influence of nuclear fluctuations on Magnetic Quantum Tunneling

Oren Shafir

Investigating the influence of nuclear fluctuations on magnetic quantum tunneling

RESEARCH THESIS

SUBMITTED IN PARTIAL FULFILLMENT OF THE
REQUIREMENTS FOR THE DEGREE OF
DOCTOR OF PHILOSOPHY

OREN SHAFIR

SUBMITTED TO THE SENATE OF THE TECHNION - ISRAEL INSTITUTE OF TECHNOLOGY
NISAN , 5769 HAIFA APRIL, 2009

The research thesis was done under the supervision of Prof. Amit Keren in the faculty of physics.

I am deeply grateful to Prof. Amit Keren for his excellent guidance, his support and encouragement throughout this period.

I thank Prof. E. Polturak and Prof. M. Reznikov for their help with the DR.

I am grateful for the big help from the lab technicians – Yoseph Direktovitch, Galina Bazalitzky, Shmuel Hoida and Dr. Leonid Iomin.

Thanks to all my friends in the research group of magnetism and Low temperatures.

Special and final thank to Bilha, for standing beside me

The generous financial help of the Technion is gratefully acknowledged

Contents

Abstract 6

Molecular magnets and quantum tunneling 10

- Introduction- Molecule Magnets (MM) 10
- The spin Hamiltonian approach 11
- Introduction to quantum tunneling of the magnetization in MM 12
- The Fe8 system 13
- The Landau Zener model 16
- The nuclear effect on the QT 18
- Our research question 20

QTM in Fe8 - Previous Works 21

- Magnetization of Fe8 22
- Evidence to the Role of Nuclei in QTM 23
- Other relevant NMR data of Fe8 24

Experimental method 27

- Sample preparation 27
- Faraday force magnetometer 30
- Dilution Refrigerator 34
- The Nuclear Magnetic Resonance (NMR) Technique 36

Experimental results 41

- Magnetization measurements 41
- ^{1}H NMR Measurements 44
- Magnetization Measurements with RF 46
- Electromagnetic radiation 47

Simulation of QTM with stochastic field 52

- Results with stochastic field, B(t) || z 52

Discussion and summary 55

- Magnetization and RF 55
- Electromagnetic radiation and Super Radiance 56

References 59

List of figures

Figure 1-1: Energy levels for a spin state S with easy axis magnetic anisotropy. The +*M* levels are localized in the left side and the -*M* levels in the right side. a) In zero field the two states are equally populated; b) the application of a magnetic field selectively populates the right side. 14

Figure 1-2: Zeeman diagram of the 21 levels of the *S*=10 manifold of Fe8 as a function of the field applied along the easy axis. From the bottom to the top, the levels are labeled with quantum numbers *M*=±10,±9,...,0. The inset displays in detail a two level crossing where the transverse terms (terms containing S_x and/or S_y spin operators) turn the crossing into an avoided crossing (from [12]). 15

Figure 1-3: Landau-Zener transition probability as a function of normalized time for three values of $\gamma = t_T/t_Z$: 0.05 (top), 0.4 (middle) and 5 (bottom). We use γ notation as in ref [17]. 17

Figure 1-4: Internal dipolar fields change the energies of the two levels split by the tunnel interaction, and thus hinder tunneling. By effectively broadening the levels, hyperfine interactions restore the matching of the left and right levels, and thus allow tunneling. 19

Figure 2-1: Structure of the molecular nanomagnet Fe8: (a) molecular view - the spin structure is schematized by the arrows [25]; (b) crystal shape - schematic view of the anisotropy axes and the crystal axes [12]. 22

Figure 2-2: Temperature (a) and field sweeping rate (b) dependence of hysteresis loops of Fe8 molecular clusters. Resonant tunneling is evidenced by equally separated steps of ΔH_z~0.22 T which, at *T*=360 mK, correspond to tunnel transitions from the state *M*=-10 to *M*=10-*n*, with *n*=0,1,2,... . The resonance widths are about 0.05 T, mainly due to dipolar fields between the molecular clusters (from [12]). 22

Figure 2-3: Temperature dependence of the elapsed time (Δt) needed to relax 1% of the saturation magnetization of a deuterium enriched Fe8 crystal (^{D}Fe8), of a standard crystal (stFe8), and of a ^{57}Fe enriched one (^{57}Fe8). Data taken from [27] 24

Figure 2-4: Temperature and external magnetic field dependence of the spin lattice relaxation rate T_1^{-1} and spin-spin relaxation rate T_2^{-1}. Not all the measurement were done on resonance (see frequency and field in the legend). Lines denote calculated values of T_1 (from [34]). 25

Figure 2-5: Field cool and zero field cool 1H-NMR spectra for FE8 single crystal at 150mK 29MHz. the broken lines show calculated level crossing field. From [34] 26

Figure 3-1: Photograph of Fe8 single crystals. 29

Figure 3-2: Principle of measurement. The magnetic force F exerted on a sample situated in a spatially varying field is detected as a capacitance change of the parallel-plate variable capacitor, whose movable plate is suspended by elastic springs S [37]. 30

Figure 3-3: Cross sectional view of the Faraday balance with: (1) movable plate of the capacitor, (2) screw for capacitor's fixed plate height adjustment, (3) sample, (4) PCTFE, (5) gold plated casing of the thermometer, (6) thermal link to the DR mixing chamber, (7) main coil, (8) gradient coils, (9) RF coil. 31

Figure 3-4 : The response of the load cell to weight at room temperature. 32

Figure 3-5 : Schematic view of the load cell device, installed off-center of a solenoid magnet in a dilution refrigerator. 33

Figure 3-6: Phase diagram of ^{3}He/^{4}He [41]. 34
Figure 3-7: Schematic diagram of a dilution refrigerator [41]. 35
Figure 3-8: Resonance circuit for the NMR probe 37
Figure 3-9: A scheme of NMR pulse sequence for the measurement of T_1. The nuclear magnetization along the applied field (shown as dashed curve) is recovered after saturation pulses. The spin echo is formed at the time t after the 180° pulse, where t denotes the time between 90° pulse and 180° pulse. 39
Figure 4-1: Capacitance Vs. Magnetic field at base temperature. The slope in the positive magnetic field is due to the gradient from the external field. The clear steps indicates the jumps in the magnetization. 41
Figure 4-2: Capacitance Vs. Magnetic field at base temperature with different sweep rates. 43
Figure 4-3: Capacitance vs. Magnetic field with sweep rate of 0.5T/min at different temperatures. The indicating temperature is of the mixing chamber, so the temperature of the sample is higher. 43
Figure 4-4: Echo intensity as a function of field (right) and pulse width (left). 44
Figure 4-5: T_2 measurements for several temperatures. 45
Figure 4-6: T_1 measurements for base temperature. 45
Figure 4-7: scheme of the measurements with RF. We sweep the magnetic field from positive to negative, and stop for several seconds to transmit the RF at 0.3T. We see that the temperature rise due to the transmitting is low, and the first two jumps are in the regime of the T_1. 46
Figure 4-8: Capacitance (=Magnetization) measurement with and without RF. We saturate the nuclei and see no effect. 47
Figure 4-9: (a) capacitance (which represents magnetization) and (b) temperature vs. magnetic field swept from positive to negative. Steps in the capacitance indicate QTM in the sample. Spikes in the temperature indicate energy bursts. 48
Figure 4-10: (a) Normalized derivative of the magnetization extracted from the capacitance (see text) and (b) temperature spikes vs. magnetic field swept from positive to negative. The changes in the magnetization are followed by an increase in the temperature, indicating release of energy. 49
Figure 4-11: Test cases: The capacitance (a) and temperature (b) vs. magnetic field swept from positive to negative with jammed capacitor. The rise in the temperature indicates the change in the magnetization. The normalized derivative of the magnetization (c) and temperature (d) vs. magnetic field (same sweeping direction) with covered sample. The change in the magnetization is not followed this time by an increase in the temperature. 50
Figure 5-1: Simulation results for various parameters with B(t) || z. the black points are analytical calculations. 54

Abstract

Molecular clusters of paramagnetic metal ions have been widely investigated as a model for magnetism at the nanoscale, especially for quantum effects such as the tunneling of the magnetic moment. The molecular magnet Fe8, is a representative compound in which quantum tunneling of magnetization (QTM) has been observed.

The main objective of this work is to observe the effect of the nuclear spins on the QTM in Fe8 by examining the influence of radio frequency (RF) on its hysteresis loop. RF pulse sequence can change the nuclear spin temperature without changing the electron spin temperature. In our experiment we measure the magnetization curve in the presence of RF, unfortunately we see no effect. This puts an experimental limit on theory.

As a by product of our experiment, we discovered a jump in the temperature every time there is a step in the magnetization curve. We present results which show that the origin of those jumps is not from the moving parts of the system, but from the sample. Others measurements show that the thermometer heats up from bursts of photons from the sample, rather than phonons. We consider in the discussion the possibility of observing super-radiance.

List of Symbols and abbreviations

Symbol	Meaning
QTM	quantum tunneling of magnetization
MM	Molecular magnets
EPR	electron paramagnetic resonance
DR	dilution refrigerator
ZF	zero field
J	magnetic coupling between ions inside a high spin molecule
S	quantum number of the total spin at the ground state
S_z	spin component in the z direction
$\mathcal{H}$	spin Hamiltonian
D	anisotropy parameter of the uniaxial term
E	anisotropy parameter of the rhombic term
k_B	Boltzmann constant, 1.38066×10^{-23} [J]/[K]
T	Temperature
$\mathbf{H}$	external magnetic field
H_x	the x component of the external magnetic field
H_m	matching field
$\mathbf{B}$	magnetic flux density
m	quantum number of the spin in the z direction
g	the spectroscopic splitting factor
μ_B	Bohr magneton, 9.274×10^{-24}[J]/[T]
$\mathbf{M}$	Magnetization
P	tunneling probability

Symbol	Meaning
ω	Frequency
$\hbar$	Plank's constant, 1.05457×10^{-34}[J][s]
t	Time
$\Delta_{m,m'}$	tunnel splitting
C	Capacitance
C_0	initial capacitance
A	area of the capacitor plates
I	moment of inertia
$\mathbf{F}$	Force
δ	displacement of the capacitor plate
d	distance between the capacitor plates
ε_0	permittivity of vacuum, 8.85419×10^{-12} [F]/[m]
E_y	Young's modulus
SR	Super-radiance
NMR	Nuclear magnetic resonance
γ	gyromagnetic ratio

Chapter 1

Molecular magnets and quantum tunneling

In this chapter we will first introduce the molecular magnet Fe8 and the concept of molecular magnets. Then we will try to explain the Hamiltonian of the system, the model of Landau and Zener for two level system, and the role of the nuclei in the tunneling process. In the end of this chapter we will present the research question.

Introduction- Molecule Magnets (MM)

Recently, molecular nanomagnets have attracted much attention in the study field of quantum mechanical phenomena occurring in macroscopic systems, owing to their identical size, well defined structure, and a well-characterized energy structure. The molecular magnet $[(C_6H_{15}N_3)_6Fe_8O_2(OH)_{12}]Br_7(H_2O)Br\cdot 8H_2O$, abbreviated Fe8, is a representative compound in which quantum tunneling of magnetization (QTM) has been observed, in the form of temperature independence, regularly spaced steps in the hysteresis loop [1, 2]. This field was investigated intensively and shows promise for its possible future applications. Some of these are in quantum computation [3, 4], as multi-bit magnetic memory [5], as an essential part in spintronics [6] and as an MRI contrast [7].

Fe8 belongs to a family called Molecule Magnets (MM). MM are molecules consisting of ions coupled by ferromagnetic or anti-ferromagnetic interactions; these molecules crystallize in a lattice where neighboring molecules are very well separated. At temperatures lower than the magnetic coupling J between ions inside the molecule, the spins of the ions are locked, and the molecules behave like non-interacting giant spins. The energy difference between the ground spin state and the next excited spin state is of the order of J, and therefore at low temperatures only the ground spin state S is populated. This state is $2S+1$ times degenerate. However, at even lower temperatures the degeneracy can be removed by additional magneto-crystalline anisotropic interactions such as the uniaxial term. When the temperature is high enough, transitions between spin states, with different S_z, are thermally activated. However, when the temperature is much lower than the energy difference between these spin states, the transitions are possible only through tunneling.

1.1 The spin Hamiltonian approach

It is often a good approximation to assume the crystal field spin Hamiltonian to have a quadratic form in the spin operator [8], i.e.

Eq. 1-1 $$\mathcal{H} = \mathbf{S} \cdot \mathbf{D} \cdot \mathbf{S}$$

where **D** is a real, symmetric tensor. If the coordinate axes x, y, z are chosen parallel to its orthogonal eigenvectors, D is diagonal and Eq. 1-1 takes the form

Eq. 1-2 $$\mathcal{H} = D_{xx} S_x^2 + D_{yy} S_y^2 + D_{zz} S_z^2$$

Where S_x, S_y, S_z are spin Operators.

Subtracting $(1/2)(D_{xx} + D_{yy})(S_x^2 + S_y^2 + S_z^2) = (1/2)(D_{xx} + D_{yy})S(S+1)$, which is a constant, one obtains

Eq. 1-3 $$\mathcal{H} = DS_z^2 + E \cdot \left(S_x^2 - S_y^2\right)$$

Where

Eq. 1-4 $$D = D_{zz} - \frac{1}{2}D_{xx} - \frac{1}{2}D_{yy};\quad E = \frac{1}{2}\left(D_{xx} - D_{yy}\right)$$

In axial symmetry, $D_{xx} = D_{yy}$ and therefore E = 0, meaning that only the D parameter is needed to express the energies of the $\left(2S+1\right)$ spin levels. The Hamiltonian (Eq. 1-3) splits the $\left(2S+1\right)$ levels even in the absence of an applied magnetic field. Therefore this effect is often called zero-field splitting (ZFS).

D can be positive or negative: in the first (second) case the levels with lowest (highest) $|m|$ are the most stable. Positive D corresponds to easy-plane magnetic anisotropy, negative D to easy-axis type magnetic anisotropy.

1.2 Introduction to quantum tunneling of the magnetization in MM

The simplest model describing QTM is that of positive (up) and negati|ve (down) spin states with an energy barrier between them. When these states are coupled, spin up and down are no longer the eigenstates of the system, and the ground state is the anti-symmetric superposition of the two states, namely, $\psi_{as} = (\psi_{down} - \psi_{up})/2$. This state is separated by a tunnel splitting energy Δ from the symmetric wave function $\psi_{s} = (\psi_{down} + \psi_{up})/2$. This can be seen more clearly in an example of a system with spin S=1/2, however we will take the case of S=1 because the Hamiltonian of Eq. 1-3 is relevant in this case. Let us take this simple spin Hamiltonian (with negative D) in a matrix description:

Eq. 1-5 $$\mathcal{H} = \begin{pmatrix} D & 0 & E \\ 0 & 0 & 0 \\ E & 0 & D \end{pmatrix}.$$

When E=0, we get three eigenstates:

$$|up\rangle = \begin{pmatrix}1\\0\\0\end{pmatrix}, \quad |middle\rangle = \begin{pmatrix}0\\1\\0\end{pmatrix} \quad \text{and} \quad |down\rangle = \begin{pmatrix}0\\0\\1\end{pmatrix}$$

Two of them are degenerate with Energy D. However, when $E\neq 0$, the two states are coupled and the eigenvalues and the eigenvectors of the Hamiltonian are:

$$\frac{1}{\sqrt{2}}\begin{pmatrix}-1\\0\\1\end{pmatrix}, \quad \begin{pmatrix}0\\0\\0\end{pmatrix} \quad \text{and} \quad \frac{1}{\sqrt{2}}\begin{pmatrix}1\\0\\1\end{pmatrix}$$

If the initial state of the system is “up”, which is not an eigenstate anymore, there is some probability that tunneling will occur between “up” and “down” states:

Eq. 1-6 $$\left|\langle down|\exp(-i\mathcal{H}t/\hbar)|up\rangle\right|^2 = \frac{1-\cos(2Et/\hbar)}{2} = \frac{1-\cos(\Delta t/\hbar)}{2}.$$

From this equation we learn that the system will oscillate between the two states at a frequency of $2E/\hbar=\Delta/\hbar$.

1.3 The Fe8 system

Let us consider the Fe8 system with a well defined ground spin state, characterized by a large value of S=10 (see chapter 2) in an external magnetic field parallel to the easy axis of the molecules. The $\mathcal{H}_0$ Hamiltonian which ignores the E term is written as:

Eq. 1-7 $$\mathcal{H}_0 = DS_z^2 + g\mu_B H_z S_z$$

where D is a negative constant in the system of interest and H_z is the magnetic field strength in the $\hat{z}$ direction. In Fe8, the value of D/k_B is reported to be –0.275 K and -0.292 K by electron paramagnetic resonance (EPR) and neutron spectroscopy, respectively [2, 10]. The energies of the spin levels corresponding to $\mathcal{H}_0$ can be calculated as given by:

Eq. 1-8 $$\mathrm{E}(M_s) = DM_s^2 + g\mu_B M_s H_z$$

where $-S \leq M_s \leq S$. The energy levels can be plotted as shown in Figure 1-1. When no external field is applied all the levels are degenerate in pairs, except $M_S = 0$. Since D is negative the $M_S = \pm S$ levels will be lowest. In Figure 1-1 the states with positive M_S are plotted on one side of the barrier, and those with negative M_S on the other. The system can be prepared in a magnetized state by applying a strong magnetic field parallel to the $\hat{z}$ axis. If the temperature T is low and the field H_z positive, the $M_S = -10$ state will be the only one populated and the magnetization will reach the saturation value.

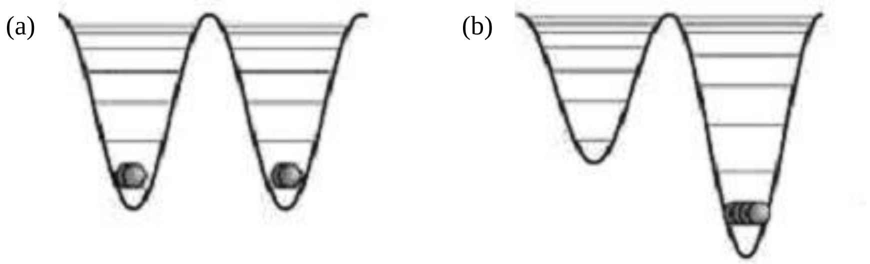

Figure 1-1: Energy levels for a spin state S with easy axis magnetic anisotropy. The +*M* levels are localized in the left side and the -*M* levels in the right side. a) In zero field the two states are equally populated; b) the application of a magnetic field selectively populates the right side.

At low temperatures only the degenerate $M_S = \pm 10$ levels will be populated, but, as long as $\mathcal{H} = \mathcal{H}_0$ (Eq. 1-7) the two states are orthogonal to each other, and there is no possibility of tunneling. In principle, since the two states are degenerate, all their linear combinations will be eigenfunctions of the system, but to observe tunneling the two states must be mixed by some suitable perturbation. Therefore, if we want to observe tunneling we must introduce the perturbation Hamiltonian $\mathcal{H}_{tr}$ that allows the mixing of the two states:

Eq. 1-9
$$\mathcal{H}_{tr} = E \cdot \left(S_x^2 - S_y^2 \right)$$

where E is a parameter determined experimentally. In Fe8, E/k_B is reported to be –0.046 K and –0.047 K by EPR and neutron spectroscopy, respectively [2, 10]. Therefore the total Hamiltonian is given by:

Eq. 1-10
$$\mathcal{H} = DS_z^2 + g\mu_B H_z S_z + E \cdot \left(S_x^2 - S_y^2 \right).$$

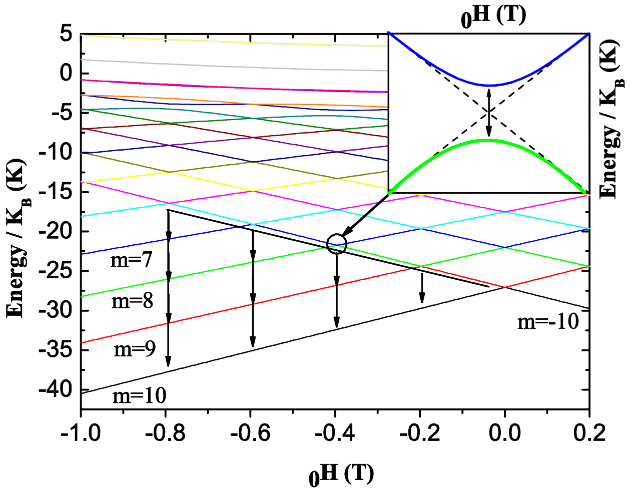

Figure 1-2: Zeeman diagram of the 21 levels of the *S*=10 manifold of Fe8 as a function of the field applied along the easy axis. From the bottom to the top, the levels are labeled with quantum numbers *M*=±10,±9,...,0. The inset displays in detail a two level crossing where the transverse terms (terms containing S_x and/or S_y spin operators) turn the crossing into an avoided crossing (from [12]).

The energy levels appropriate to the Fe8 Hamiltonian, as a function of applied magnetic field can be calculated by diagonalizing the 21×21 matrix of the 2*S*+1 states (*S*=10). The results are plotted in Figure 1-2. The field, at which crossing occurs, is given by the equation:

Eq. 1-11
$$H_m(n) = \frac{nD}{g\mu_B} \approx n \times 0.2T\,.$$

Here H_m is called “matching” or “resonance” field. At these fields, magnetizations with opposite signs have identical energies and tunneling can occur. It is easy to show that if only the parameter *D* is included, all the +M_S levels will cross the -M_S levels at the same field. This is no longer true if higher-order terms are included. In addition, as shown in the inset of Figure 1-2, the two level crossing turns into an avoided crossing with a gap Δ which is the tunnel splitting. Due to Chudnovsky and Garanin [13], this tunnel splitting Δ can be calculated for the ground state splitting (m=-S, m'=-m-k=-S-k) by:

Eq. 1-12
$$\Delta_k = g_k \left(\frac{E}{8D} \right)^{S-k/2}$$

where:

Eq. 1-13

$$g_k = \frac{8D}{\left[(S - k/2 - 1)!\right]^2} \sqrt{\frac{(2s-k)!(2S)!}{k!}} \, .$$

This is only an approximate solution, because even very small higher-order transverse couplings can make an important contribution to Δ_k. This makes Δ_k impossible to calculate. Wernsdorfer et al. [12] have measured Δ_{10} for many different sweeping rates using the Landau-Zener model (see below). Their experiment showed that $\Delta_{10} \sim 10^{-7}$K, two orders of magnitude bigger then the calculated one ($\Delta_{10} \sim 7 \cdot 10^{-10}$ K if one substitute, *D* and *E* of Fe8 in Eq. 1-12).

1.4 The Landau Zener model

The Landau–Zener (LZ) model [14, 15, 16] is an analytic solution of the equations of motion governing the transition dynamics of a 2-level quantum mechanical system, with a time-dependent Hamiltonian varying in such a way that the energy separation of the two states is a linear function of time. The model gives the probability of transition between the two energy states.

Let us use the simplest Hamiltonian appropriate for the Landau-Zener problem. It is the Hamiltonian of a spin 1/2 which has a resonance tunnel splitting Δ at $t = 0$, and a time-dependent magnetic field αt in the z direction. The Hamiltonian is given by:

Eq. 1-14

$$\mathcal{H}_0 = \alpha t S_z + \Delta S_x$$

where $S_z = \sigma_z/2$, $S_x = \sigma_x/2$ (σ_z and σ_x are the Pauli matrixes). The Schrödinger equation could be written in a dimensionless form as:

Eq. 1-15

$$i \frac{t_T}{t_z} \frac{\partial}{\partial y} \left| n \right\rangle = \left(y S_z - S_x \right) \left| n \right\rangle$$

Where $t_z = \Delta/\alpha$ is the Zener time, $t_T = \hbar/\Delta$ is the tunneling time and $y = t/t_z$ is dimensionless time.

Let us define the states $|+\rangle = [1,0]$ and $|-\rangle = [0,1]$. We are interested in the LZ probability that a spin prepared at time $t = -\infty$ in the low energy state $|+\rangle$ will be in the high energy state at $t = \infty$ which is again the $|+\rangle$ state. For this purpose we have to calculate the matrix element

$$C_{LZ} = \langle + | U | + \rangle \qquad \textbf{Eq. 1-16}$$

where U is the time propagator operator. If the Hamiltonian had been time independent, this operator would have been $e^{(-i\mathcal{H}_0 t/\hbar)}$, but it does depend on time and a more complicated and approximated expression for U will be given soon. The probability of changing energy states is given by

$$P_{LZ} = |C_{LZ}|^2 \qquad \textbf{Eq. 1-17}$$

In the standard LZ model practically no transitions take place at large negative or positive times. The transitions essentially take place within the Zener time scale t_z around t = 0. This is demonstrated in Figure 1-3 which is a numerical solution of Eq. 1-15, as a function of time for three different values γ = t_T/t_Z (our results are similar to the simulation of Mullen et. al. [17]).

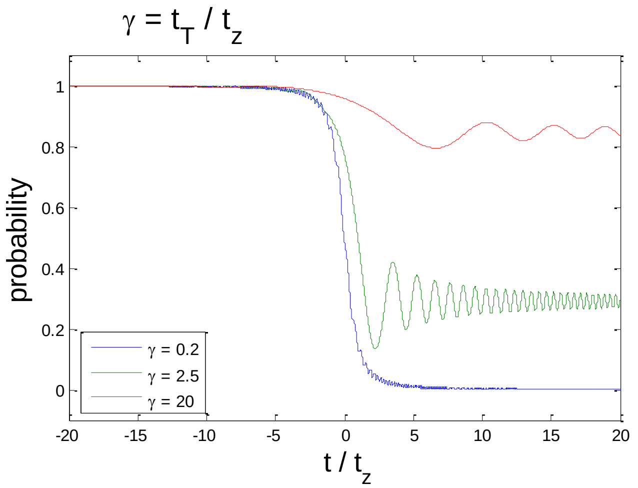

Figure 1-3: Landau-Zener transition probability as a function of normalized time for three values of γ = t_T/t_z: 0.05 (top), 0.4 (middle) and 5 (bottom). We use γ notation as in ref [17].

The asymptotic case $t = \infty$ can be solved analytically:

Eq. 1-18 $$P_{ZL} = \exp\left(-\frac{\pi\Delta^2}{2\hbar\alpha} \right) = \exp\left(-\frac{\pi t_z}{2t_T} \right)$$

In Fe8, one can take every level crossing, and use its tunnel splitting in the way that:

Eq. 1-19 $$P_{m,m'} = 1 - \exp\left[-\frac{\pi\Delta^2_{m,m'}}{2\hbar g\mu_B \left| m - m' \right| dH/dt} \right]$$

where the tunnel splitting $\Delta_{m,m'}$ takes very different values at the various resonances, as seen from Eq. 1-12.

1.5 The nuclear effect on the QT - hyperfine interactions

Similarly to Eq. 1-6, in a coherent tunneling process the wavefunction, which initially is prepared to correspond to the localized $\left| M_S \right\rangle$ state, should indefinitely oscillate as in:

Eq. 1-20 $$\left| \Psi(t) \right\rangle = \left| -M_S \right\rangle \cos(\omega t) + \left| +M_S \right\rangle \sin(\omega t)\,.$$

In incoherent tunneling (which is observed experimentally) on the other hand, the spin goes from the $\left| -10 \right\rangle$ state to the $\left| +10 \right\rangle$ and stays there.

Non diagonal terms in the Hamiltonian (Eq. 1-9) cannot explain the experimentally observed tunneling [18], because energy must be conserved during the process. In a macroscopic system, the required energy can be provided by phonons. However, phonons are not very effective of low fields and at a low temperature because of their low density of states at low energies. Another possible source of energy is the dipolar interactions between spins of different molecules. This interaction is, however, hardly compatible with energy conservation because the energy levels are discrete. Hyperfine interactions, which designate the interaction between electronic and nuclear spins, were shown to be the solution to this problem [18, 19, 20].

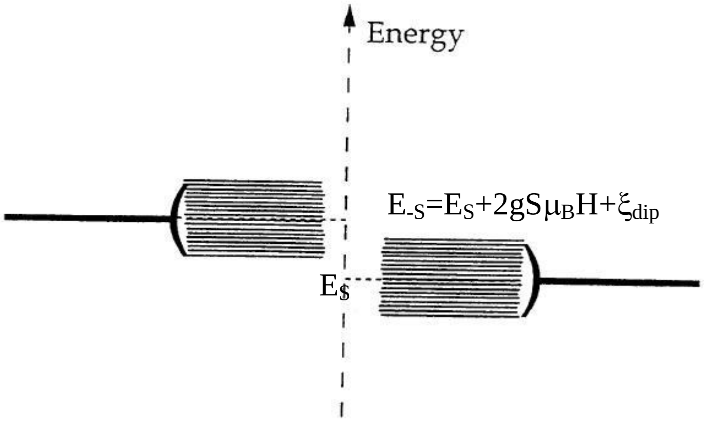

Figure 1-4: Internal dipolar fields change the energies of the two levels split by the tunnel interaction, and thus hinder tunneling. By effectively broadening the levels, hyperfine interactions restore the matching of the left and right levels, and thus allow tunneling.

At a low temperature (T < 0.4K in Fe8) only the lowest levels ±10, which are coupled by the tunneling matrix element Δ_{10}, are involved. Tunneling can occur only if $\xi < \Delta_{10}$, where $\xi = |E_S - E_{-S}|$ is the bias between the two lowest levels (Figure 1-4), which is $\xi = 2g\mu_B S|H|$ without hyperfine and dipolar fields. Since the typical bias caused by intermolecular dipolar fields alone is $\xi_{dip} \sim 0.05T$ [21] and the tunnel splitting (Δ_{10}) of the ±10 levels in Fe8 corresponds to a field of approximately 10^{-8} T [9], it seems at first that almost all molecules should not be able to tunnel. Prokof'ev and Stamp [19, 20] suggested that each molecule sees both a small, rapidly varying hyperfine field and a quasistatic dipole field due to its neighbors. For a fraction of the molecules the net dipole field will happen to be small enough for the fluctuating hyperfine fields to sweep the total field through the resonance condition, allowing it to tunnel (see Figure 1-4). Once it has tunneled, it alters the dipole fields seen by its neighbors, allowing some of them to tunnel, etc. In this theory, if $\xi = |E_S - E_{-S}| = 0$, the molecules relax (tunnel incoherently) at a rate given by [20]:

$$\textbf{Eq. 1-21} \qquad t'^{-1}_{T} \approx \frac{2\Delta^2}{\sqrt{\pi}} T_2$$

where T_2 is the time constant which describes the dephasing of the transverse nuclear magnetization, called the spin-spin relaxation time. The hyperfine bias field on a given molecule rapidly fluctuates at a rate T_2^{-1} [19]. One can take this t'^{-1}_T and place it instead of t_T^{-1} in Eq. 1-18.

Another perspective is to look for a broader LZ theory which includes stochastic fluctuations produced by the environment, or the nuclei in our case. Such a theory was developed by Shimshoni and Stern (SS) [43]. The SS theory takes into account the dephasing effect due to stochastic field fluctuations. Under the conditions [63]:

Eq. 1-22
$$\frac{\Delta}{g\mu_B\dot{h}_z} > \frac{\hbar^2}{\left\langle H_{hf}^2 \right\rangle T_2} > \frac{\hbar}{\Delta} \qquad \text{and} \qquad \frac{\hbar^2}{\left\langle H_{hf}^2 \right\rangle T_2} > T_2$$

were $\dot{h}_z$ is the sweep rate of the magnetic field in the Z direction and H_{hf} is the hyperfine field, the observed probability is given by:

Eq. 1-23
$$P_{ss} = \frac{\hbar^2}{\left\langle H_{hf}^2 \right\rangle T_2} \frac{g\mu_B\dot{h}_z}{\Delta} e^{\frac{2\left\langle H_{hf}^2 \right\rangle T_2\Delta}{\hbar^2 g\mu_B\dot{h}_z}} P_{LZ} .$$

As one can see, changing T_2 should influence the probability strongly (T_2 is in the exponent).

1.6 Our research question

LZ theory predicts transition probabilities; however, it has not been able to account for the size of the magnetization jumps in molecular magnets. In fact, the discrepancy between Δ deduced from LZ experiments [12] and the one calculated from spectroscopic data is more than two orders of magnitude [42], as we mentioned in chapter 1.3. Our research question is: what is the reason for the big difference between the calculated and the experimental value of the tunnel splitting Δ?

Our method is to change T_2 by applying RF, and see if we can affect the tunneling rate.

Chapter 2

QTM in Fe8 - Previous Works

An Fe8 molecular cluster was first synthesized in 1984 [22.] It consists of eight Fe^{3+} ions (s = 5/2), as shown in Figure 2-1(a). The magnitude of magnetic interactions between the spins of the Fe^{3+} ions in the molecule is between 20 to 170K [23], while the magnetic interactions between the molecules are much smaller. The magnetic properties of this compound at low temperatures have been described by a simple spin model with total spin of S = 10 in which six spins are parallel to each other and the remaining two spins are anti-parallel to the other spins (see Figure 2-1(a); this model was experimentally confirmed by magnetization measurements [24] and also by a polarized neutron-diffraction experiment [11]). The experimental results of the magnetization curves at low temperatures show large anisotropy that is dependent on the orientation of the external magnetic field with respect to the crystal axis [11]. The "easy axis" in Fe8 is oriented with an azimuthal angle of 16° from the *a*-axis in the *ab*-plane and an inclinational angle of 0.7° from the *ab*-plane as can be seen in Figure 2-1(b).

Fe8 is ideal for investigating quantum effects that affect the magnetization dynamics. There are several reasons for this: The biaxial anisotropy has been carefully measured [23], and a reasonably large transverse term promotes tunneling effects; in addition, the experimentally observed barrier (between spin up and down, Figure 1-1) is ~ 24 K [23] which is not too high, and apparently the samples contain only one crystallographic phase [25]. The net result is that the relaxation of the magnetization becomes temperature independent below 0.4 K, suggesting that a pure tunneling regime is attained [1]. In this regime the relaxation of the magnetization near a resonance is of the order of hours, and experiments can therefore measure a significant part of the magnetization decay.

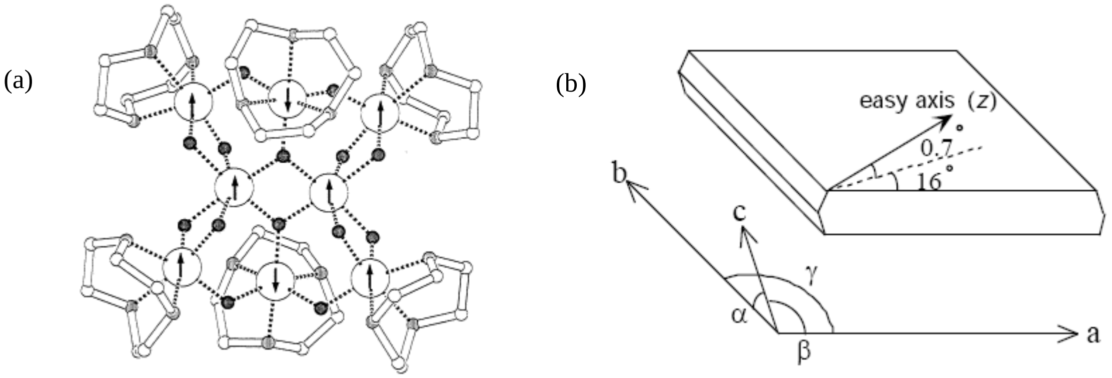

Figure 2-1: Structure of the molecular nanomagnet Fe8: (a) molecular view - the spin structure is schematized by the arrows [25]; (b) crystal shape - schematic view of the anisotropy axes and the crystal axes [12].

2.1 Magnetization of Fe8

The magnetization of Fe8 molecules as a function of external field is presented in Figure 2-2, exhibiting hysteresis and steps at well defined field values [12].

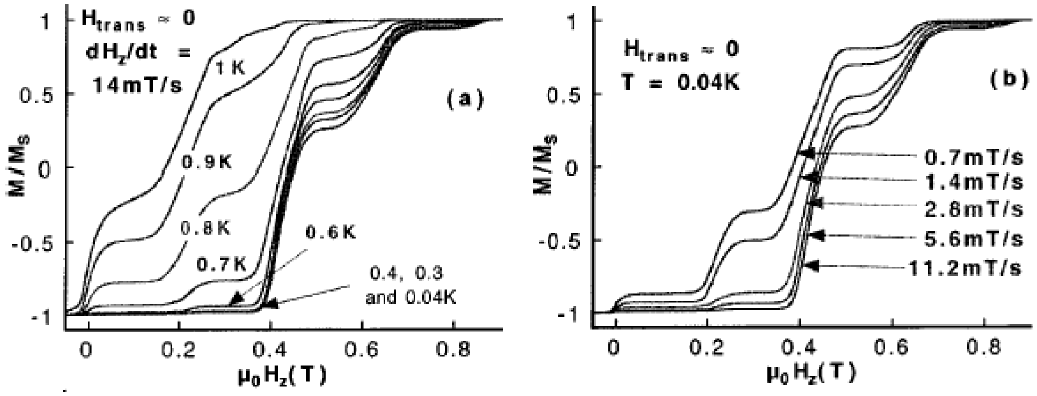

Figure 2-2: Temperature (a) and field sweeping rate (b) dependence of hysteresis loops of Fe8 molecular clusters. Resonant tunneling is evidenced by equally separated steps of ΔH_z~0.22 T which, at T=360 mK, correspond to tunnel transitions from the state M=-10 to M=10-n, with n=0,1,2,... . The resonance widths are about 0.05 T, mainly due to dipolar fields between the molecular clusters (from [12]).

On the left side (Figure 2-2a) one can see the dependence on the temperature of the 'staircase' structure above 0.4 K and at a constant sweep rate. On the right side (Figure 2-2(b)), five curves taken at 40 mK are shown, with five different ramping rates. The steps for all ramping rates occur at the same field values, but the size of the step is different for different ramping rates.

2.2 Evidence to the Role of Nuclei in QTM

The influence of nuclear spins on resonant quantum tunneling in Fe8 was demonstrated by comparing the relaxation rate of the standard Fe8 sample with two isotopic modified samples [26, 27]: (i) ^{56}Fe is replaced by ^{57}Fe, and (ii) a fraction of ^{1}H is replaced by ^{2}D. Enrichment with ^{57}Fe shortens the relaxation time, in agreement with the increased hyperfine field ($I_{^{57}Fe} = 1/2, I_{^{56}Fe} = 0$), while the enrichment with deuterium ($I_H = 1/2$, $\gamma_H = 42.576[MHz]/[T]$, $I_D = 1$, $\gamma_D = 6.535[MHz]/[T]$) causes an increase of the relaxation time, in agreement with the decreased hyperfine field (Figure 2-3). This unusual isotope effect, which is not related to the mass (which is increased in both isotopically modified samples), seems to be related to the broadening of the tunneling resonance [21] as confirmed by the investigation of the intrinsic linewidth by the hole-digging technique [28]. The linewidth is larger for the ^{57}Fe enriched sample and smaller for the deuterated one. The observed linewidth for the natural-abundance derivative is in qualitative agreement with the hyperfine fields of the protons determined by NMR spectroscopy [29, 30]. The increase in linewidth observed in the enriched sample compares well with an approximation performed taking into account the contact term of the hyperfine interaction of ^{57}Fe nuclei in iron (iii) systems.

It should be pointed out that the same group measured also the hysteresis loops of those isotopes below 1.5K, but no change of the relative positions of the tunneling resonance as a function of the longitudinal field H_z was seen [27]. A quantitative measurement of this kind is complicated by the fact that it is impossible to have two crystals with exactly the same shape, i.e. the same internal fields. As we explain later our technique solves this problem since it works with one sample only.

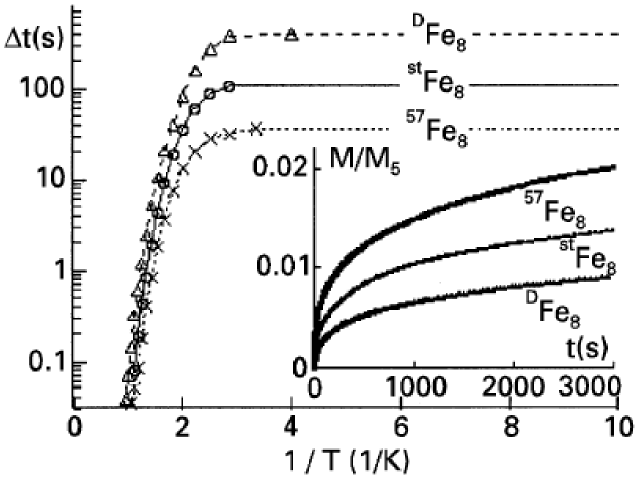

Figure 2-3: Temperature dependence of the elapsed time (Δt) needed to relax 1% of the saturation magnetization of a deuterium enriched Fe8 crystal (^{D}Fe8), of a standard crystal (stFe8), and of a ^{57}Fe enriched one (^{57}Fe8). Data taken from [27]

2.3 Other relevant NMR data of Fe8

A few studies were done on Fe8 by ^{1}H NMR [29, 30, 31, 32, 33], above 1.5K. The NMR spectra showed the presence of several lines shifted by several MHz from the Larmor frequency. The shifted lines appeared gradually as the temperature was lowered below about 10–15 K. They found that the criteria according to which the shifted lines should be observed is that the low lying $m=\pm10$ magnetic levels are sufficiently populated, and that their lifetime due to intra-well transitions becomes longer than the reciprocal of the interaction frequency (10^7 sec^{-1}). Maegawa and Ueda also measured the spin-spin relaxation rate T_2^{-1} as a function of temperatures [34, 35], as one can see in Figure 2-4, and also as a function of field in low temperatures. Moreover, their measurements in low temperatures showed a wide line of the NMR signal, with a full width half maximum of ~0.2T (Figure 2-5).

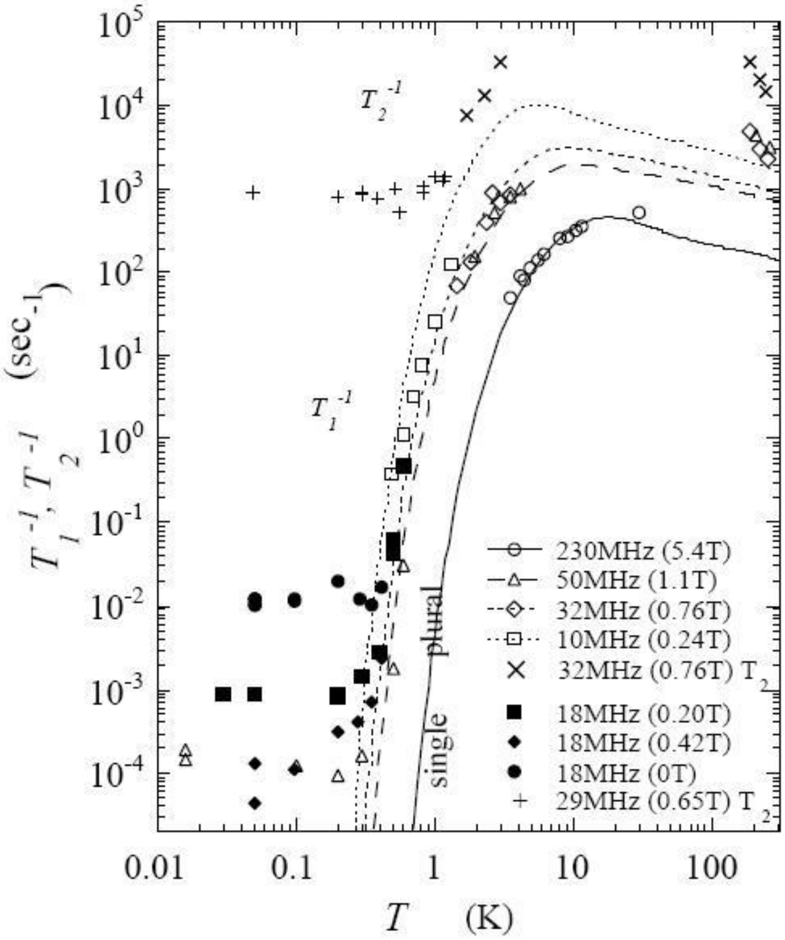

Figure 2-4: Temperature and external magnetic field dependence of the spin lattice relaxation rate T_1^{-1} and spin-spin relaxation rate T_2^{-1}. Not all the measurement were done on resonance (see frequency and field in the legend). Lines denote calculated values of T_1 (from [34]).

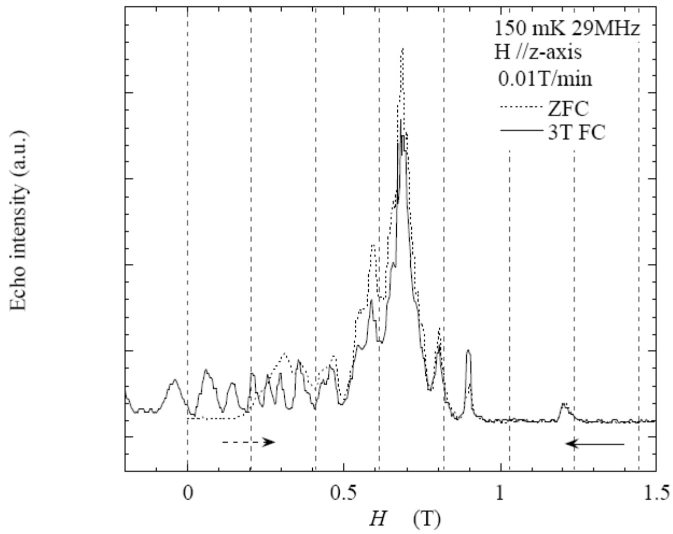

Figure 2-5: Field cool and zero field cool 1H-NMR spectra for FE8 single crystal at 150mK 29MHz. the broken lines show calculated level crossing field. From [34]

Chapter 3

Experimental Method

We prepared Fe8 crystals and measure their magnetization as a function of the magnetic field at sub-Kelvin temperature after exciting the nuclear states and raising their temperature (using RF). Due to the long T_1 (~10,000 sec) the nuclei remain excited during the magnetization experiment. The magnetic measurements are made using a Faraday force magnetometer.

3.1 Sample preparation

Single crystals of $[(C_6H_{15}N_3)_6Fe_8O_2(OH)_{12}]Br_7(H_2O)Br\cdot 8H_2O$, were synthesized through the following steps:

Synthesis of $(C_6H_{15}N_3)FeCl_3$ [36]

1.6 ml of ethanol with 0.2g 1,4,7-triazacyclononane (tacn) is added to a solution of $FeCl_3\cdot$6H2O (0.45 g) in ethanol (12.8 ml). The resulting bright yellow precipitate of $(tacn)FeCl_3$ is filtered off, washed with ethanol, and air-dried (0.35 g).

Synthesis of Fe8 [22]

0.35g of (tacn)FeCl3 was dissolved in 28 ml H2O and 2.8 ml pyridine, while rotating the entire solution for about 15 min. Then 7g of NaBr was added to the solution. Contrary to Wieghardt et. al. [22], nothing happened after 24 hours. After two-three weeks, brown crystals of Fe8, $[(C_6H_{15}N_3)_6Fe_8O_2(OH)_{12}]Br_7(H_2O)Br\cdot 8H_2O$, separated out. The maximum size of the synthesized single crystals are about 3×2×1 mm3. It is possible to add to the solution (after the NaBr) one single crystal of Fe8 and then one can obtain a bigger single crystal (8×6×1.5 mm3).

3.1.1 Chemical analysis

The sample was sent to the microanalysis lab (Hebrew University) for chemical analysis. The results of the analysis were:

Element	**Carbon (C)**	**Hydrogen (H)**	**Nitrogen (N)**	**Brome (Br)**
% calculated	20.6	4.8	12	28.41
% found	18.68	5.19	10.64	28.14

Table 3.1.1: The results of chemical microanalysis of Fe8

3.1.2 X-ray crystallography analysis

A small fragment from a large crystal was mounted on the Nonius Kappa CCD diffractometer using Mokα radiation at ambient temp. Cell parameters were obtained from ten frames as follows:

a = 10.64Å, b = 14.12Å, c = 15.09Å, $\alpha = 89.64^0$ $\beta = 70.01^0$ $\gamma = 70.80^0$. By shift of origin by one translation along a axis, the following cell parameters are obtained: a = 10.64Å, b = 14.12Å, c = 15.09Å, $\alpha = 89.64^0$ $\beta = 109.99^0$ $\gamma = 109.20^0$. These parameters are rather close to those given by Wieghardt et al. at 243 K [22] as shown the following table:

Crystal parameters	**a [Å]**	**b [Å]**	**c [Å]**	**α**	**β**	**γ**
Wieghardt et al.[6] (243K)	10.522	14.05	15.00	89.90°	109.65°	109.27°
X-ray crystallography Analysis (27°C)	10.64	14.12	15.09	89.64°	109.99°	109.20°

Table 3.1.2: The results of X-ray crystallography analysis

A schematic view of Fe8 single crystal and its crystallographic axes are shown in Figure 2-1.

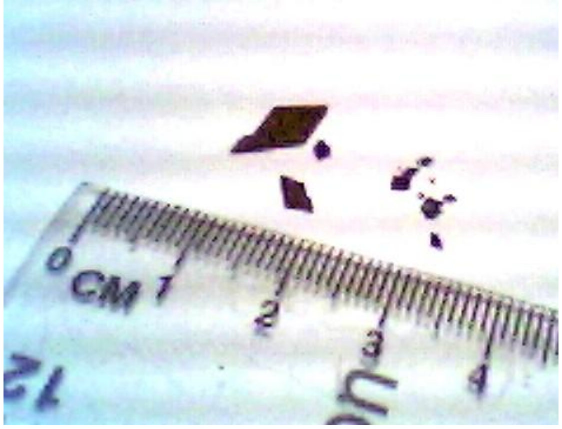

Figure 3-1: Photograph of Fe8 single crystals.

An attempt to prepare the samples under high magnetic fields (up to 8 Tesla) did not change the crystals.

3.2 Faraday force magnetometer

A Faraday force magnetometer was designed for magnetization measurement at very low temperatures following Sakakibara et al. [37]. The magnetic force acting on a specimen located in the inner vacuum chamber (IVC) of a dilution refrigerator (DR) is detected by a load sensing variable capacitor.

This method has been chosen because: (I) It fits magnetic measurements in high fields and at sub-Kelvin temperatures. (II) It can be used with no metallic parts near the sample (no coils). This is important because we want to minimize heating metallic parts with the RF.

3.1.1 Method of measurement

A sample of magnetization **M** is mounted on a small load-sensing device (≡ load cell) made of a parallel plate variable capacitor, whose movable plate is suspended by elastic springs (Figure 3-2). When the sample is subjected to a spatially varying magnetic field **B**, it will experience a force [38]

Eq. 3-1 $$\mathbf{F} = (\mathbf{M} \cdot \nabla)\mathbf{B}\,.$$

If **F** is directed perpendicular to the plates, the movable plate will then be pushed until the restoring force of the springs balances **F**. Within an elastic deformation of the springs, the displacement of the plate is proportional to **F** and can be detected as a capacitance change ΔC.

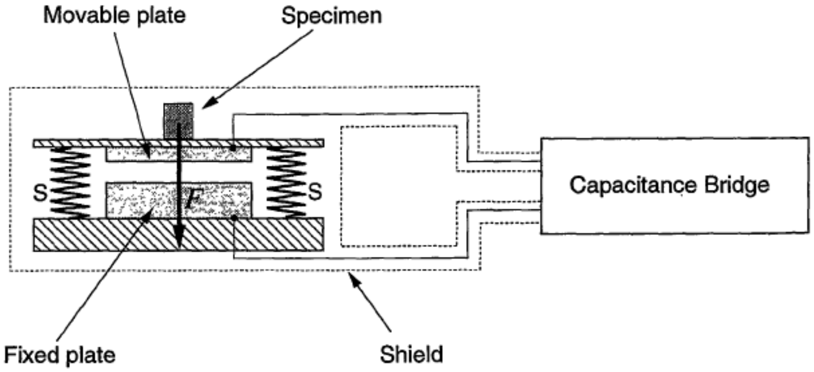

Figure 3-2: Principle of measurement. The magnetic force F **exerted on a sample situated in a spatially varying field is detected as a capacitance change of the parallel-plate variable capacitor, whose movable plate is suspended by elastic springs S [37].**

The natural field-gradient at the off-center position of a solenoid magnet will be used (Figure 3-5) [39]. It is reasonable to assume that the sample is small enough for **M** not to vary spatially. If we neglect the radial term (because $M_r << M_z$, $B_r << B_z$, and because of the properties of the load cell), from Eq. 3-1 the force on the load cell is:

Eq. 3-2 $$\mathbf{F} = M_z \frac{dB_z}{dz}\hat{z}.$$

The total capacitance response is then given by:

Eq. 3-3 $$C_0^{-1} - C^{-1} = a \cdot M_z \frac{dB_z}{dz}$$

where a is a constant that dependents on the elastic properties of the wires.

3.2.2 Design and performance of the load cell

The load cell is shown in Figure 3-3. The movable plate, on which the sample is mounted, is made of epoxy (stycast #1266), with its metallized surface facing down toward the fixed plate. The diameter of the two plates is 16mm and the unloaded capacitance with a gap of $d = 0.4mm$ is $C = \varepsilon_0 A/d \approx 5$pF (where A is the area of the plate and ε_0 is the permittivity of vacuum).

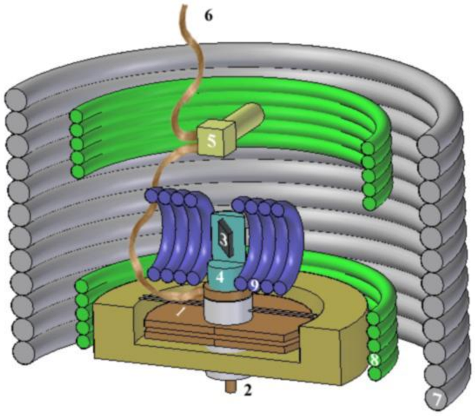

Figure 3-3: Cross sectional view of the Faraday balance with: (1) movable plate of the capacitor, (2) screw for capacitor's fixed plate height adjustment, (3) sample, (4) PCTFE, (5) gold plated casing of the thermometer, (6) thermal link to the DR mixing chamber, (7) main coil, (8) gradient coils, (9) RF coil.

The movable plate is attached to four pairs of orthogonal crossed wires (0.2mm diameter) of phosphor bronze, strung with a tension of ~0.5N. The static plate was mounted on an epoxy screw, for adjusting the initial capacity (by adjusting the initial gap between the capacitor plates).

The displacement δ of a capacitor plate caused by a force F_z can be estimated using the formula [37]:

Eq. 3-4 $$\delta / F_z = L^3 / 192 n E_y \cdot I$$

where n and L are the number and the effective length of the wires (respectively), E_y is Young's modulus, and I is the moment of inertia ($I = \pi D^4 / 64$) of the wire with a diameter D. From the actual values (L=10mm, D=0.2mm, E_y~1×10^{10} N/m^2), the response of the load cell can be estimated to be $\delta / F_z \sim 0.2 mm / N$, or when $C_0 \sim 5 pF$: $\Delta C / F_z \sim 30 pF / N$ (It is noted that ΔC is not linear with respect to force, especially above $\Delta C / C_0 \sim 0.1$) which , as we shell see, is not a problem in our case.

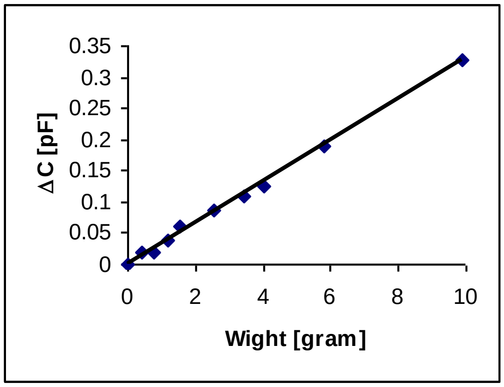

Figure 3-4 : The response of the load cell to weight at room temperature.

Neglecting edge effects of the capacitor, ΔC can be transformed to the displacement δ of the plate by the simple formula:

Eq. 3-5 $$\delta = \varepsilon_0 A (C_0^{-1} - C^{-1})$$

where A denotes the area of the plates, ε_0 is the permittivity of vacuum and $C = C_0 + \Delta C$.

3.3.2 Measuring the temperature

We chose the thermal link to be kel-f (or PCTFE: Poly-Chloro-TriFluoro-Ethylene), a fluorocarbon-based polymer which has no H^1 atoms and is suitable for Cryogenic applications. (Figure 3-3).

For thermal connection between the sample and the holder (kel-f) we used GE-Varnish which is known as reasonable heat conductor at low temperature. The bottom of the kel-f, which is outside of the coil, was connected to the copper plate. A copper braid connected the thermometer with the copper plate on the load cell as shown in (Figure 3-3). We measured the temperature with a RuO_2 2200 resistance thermometer (using kithley 2000), which we mounted ~2cm above the sample.

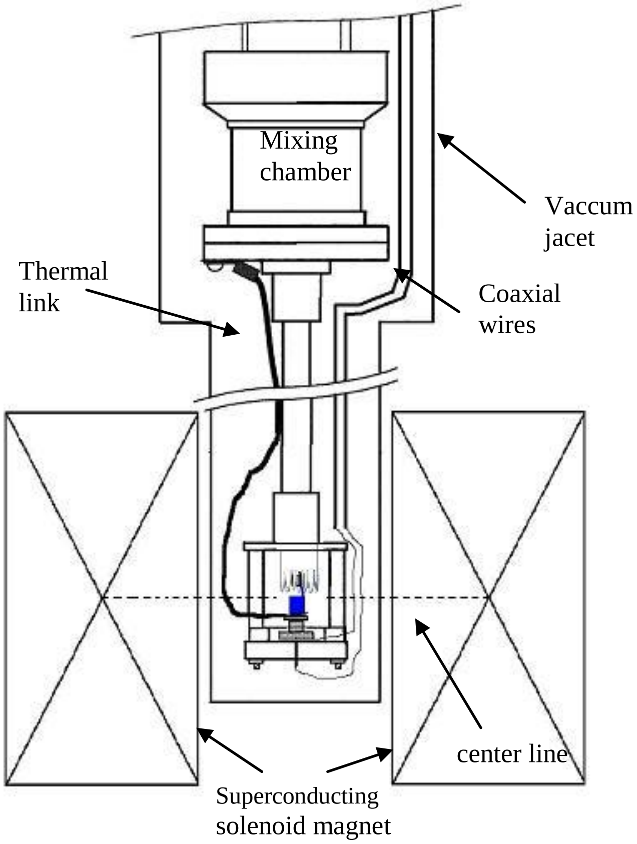
Mixing
chamber
Vaccum
jacet
Thermal
link
Coaxial
wires
center line
Superconducting
solenoid magnet

Figure 3-5 : Schematic view of the load cell device, installed off-center of a solenoid magnet in a dilution refrigerator.

3.3 Dilution Refrigerator

The ^{3}He-^{4}He dilution refrigerator (DR) was used for all the measurements at the sub-Kelvin temperature range. The principle of operation of the DR was originally proposed by H. London in 1962 [40]. When a mixture of the two isotopes of helium is cooled below a critical temperature, it separates into two phases as shown in Figure 3-6. The higher (or lighter) "concentrated phase" is rich in ^{3}He and the heavier "dilute phase" is rich in ^{4}He. The concentration of ^{3}He in each phase depends upon the temperature. Since the enthalpy (the sum of the internal heat in a system and the product of its volume and pressure) of the ^{3}He in the two phases is different, it is possible to cool the system by "evaporating" the ^{3}He from the concentrated phase into the dilute phase. Although the properties of the liquids in the DR are described by quantum mechanics, it is possible to understand the cooling process in a classical way: let's regard the concentrated phase of the mixture as liquid ^{3}He, and the dilute phase as ^{3}He 'gas' which moves through the liquid ^{4}He without interaction. This 'gas' is formed in the mixing chamber at the phase boundary. This process continues to work even at the lowest temperatures because the equilibrium concentration of ^{3}He in the dilute phase is still finite, even as the temperature approaches absolute zero.

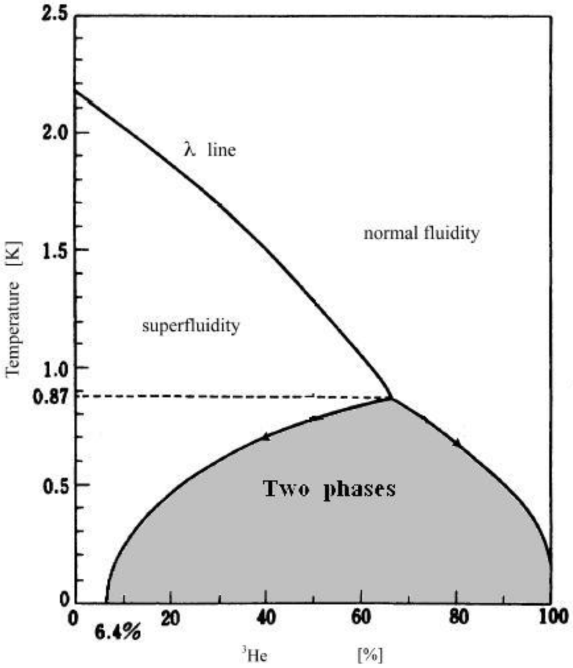

Figure 3-6: Phase diagram of ^{3}He/^{4}He [41].

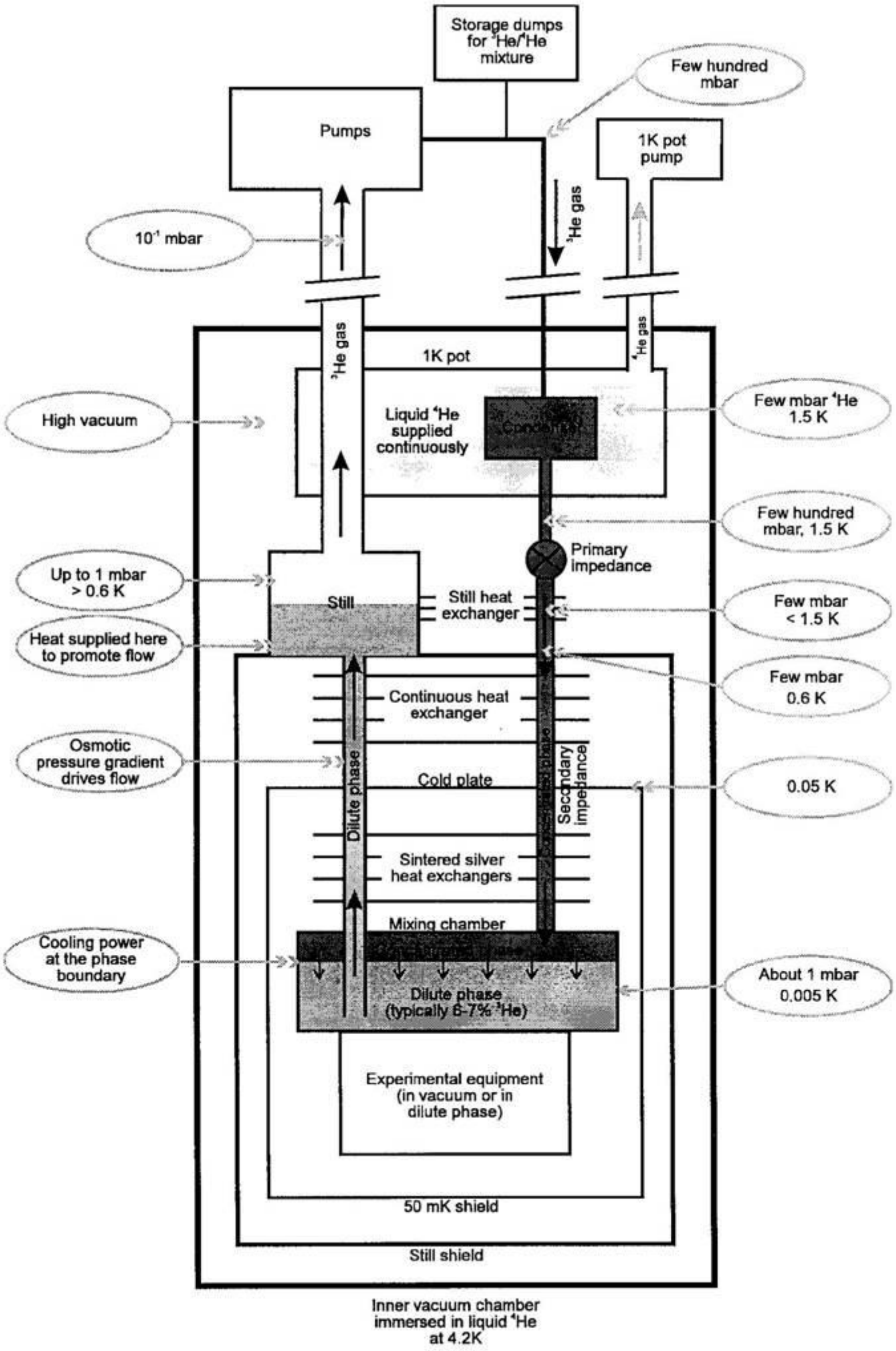
Storage dumps for ^{3}He/^{4}He mixture
Few hundred mbar
Pumps
1K pot pump
10^{-1} mbar
^{3}He gas
^{3}He gas
^{4}He gas
1K pot
High vacuum
Liquid ^{4}He supplied continuously
Condenser
Few mbar ^{4}He 1.5 K
Few hundred mbar, 1.5 K
Primary impedance
Up to 1 mbar > 0.6 K
Still
Still heat exchanger
Few mbar < 1.5 K
Heat supplied here to promote flow
Few mbar 0.6 K
Continuous heat exchanger
Osmotic pressure gradient drives flow
Dilute phase
Concentrated phase
Secondary impedance
Cold plate
0.05 K
Sintered silver heat exchangers
Mixing chamber
Cooling power at the phase boundary
Dilute phase (typically 6-7% ^{3}He)
About 1 mbar 0.005 K
Experimental equipment (in vacuum or in dilute phase)
50 mK shield
Still shield
Inner vacuum chamber immersed in liquid ^{4}He at 4.2K

Figure 3-7: Schematic diagram of a dilution refrigerator [41].

A schematic diagram of a DR is shown in Figure 3-7. When the refrigerator is started the 1K pot is used to condense the ^{3}He/^{4}He mixture into the dilution unit. It is not intended to cool the mixture enough to set up the phase boundary but only to cool it to ~1.5K. The still is the first part of the fridge to cool below 1.5 K due to its own pump. It cools the incoming ^{3}He before it enters the heat exchangers and the mixing chamber, and phase separation typically occurs after a few minutes (below 0.87 K). If the ^{3}He concentration in the mixture is good, the phase boundary is inside the mixing chamber, and the liquid surface is in the still.

^{3}He is pumped away from the liquid surface in the still, which is typically maintained at a temperature of 0.6 to 0.7 K. At this temperature the vapor pressure of ^{3}He is about 1000 times higher than that of ^{4}He, so ^{3}He evaporates preferentially. A small amount of heat is supplied to the still to promote the required flow. The concentration of ^{3}He in the dilute phase in the still therefore becomes lower than it is in the mixing chamber, and the osmotic pressure difference drives a flow of ^{3}He to the still. The ^{3}He leaving the mixing chamber is used to cool the returning flow of concentrated ^{3}He in a series of heat exchangers (sintered silver heat exchangers are used to decrease the thermal boundary resistance between the liquid and the solid walls).

The room temperature vacuum pumping system is used to remove ^{3}He from the still, and compress it to a pressure of a few hundred millibars.

The experimental apparatus is mounted on or inside the mixing chamber, ensuring that it is in good thermal contact with the diluted phase.

3.4 The Nuclear Magnetic Resonance (NMR) Technique

During the measurement of the magnetization we transmit RF pulse sequence. The RF power is delivered to the RF coil by an independent coaxial cable, as showed in Figure 3-3 (see also section 4.2).

In an NMR experiment the sample is placed inside a coil, and immersed in a static external magnetic field $H = H_0 \hat{z}$ (see Figure 3-8). This field polarizes the nuclear spins along the z axis. In addition to this field we apply a transverse magnetic field H_1 along the x axis, which is produced by running an alternating current in the coil L, with frequency equal to the Larmor frequency, $\omega_L = \gamma_N H_0$, where γ_N is the gyromagnetic ratio of the studied nuclear spin. To do so we tune the resonance frequency of the circuit by changing the capacitance of both capacitors C and C_0. We keep the impedance of the power supply (50 Ω) matched to the impedance of the rest of the circuit, in order to get maximum power from the power supply into the circuit. To ensure these two conditions, one must have:

Eq. 3-6
$$C + C^{'} = \frac{1}{\omega_L L}$$

Eq. 3-7
$$\frac{50}{R} = \left(1 + \frac{C}{C^{'}}\right)^2$$

where R is assumed to be small.

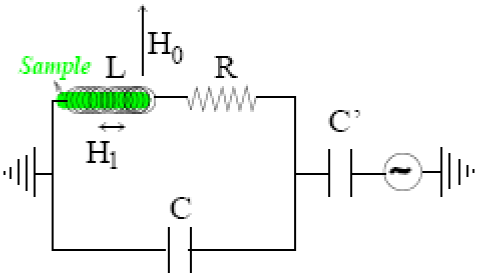

Figure 3-8: Resonance circuit for the NMR probe

To understand the effect of H_1 on the nuclear spins, it is convenient to define a rotating frame of reference which rotates about the z axis at the Larmor frequency, ω_L. We distinguish this rotating coordinate system from the laboratory system by primes on the x and y axes, $x^{'}$ $y^{'}$. The advantage of looking at the problem from a rotating reference frame is its simplicity; e.g. a nuclear magnetization vector rotating at the Larmor frequency in the laboratory frame appears stationary in a frame of reference rotating about the z axis.

When the alternating current through the coil is turned on and off, it creates a pulsed H_1 magnetic field along the $x^{'}$ axis, this field can be seen as the sum of two components, one rotating clockwise and the other counter clockwise. It can be shown that only the component which is stationary in the rotating reference frame is important, and is taken into account. The spins respond to this pulse in such a way in order to cause the net nuclear magnetization vector to rotate about the direction of the applied H_1 field. The rotation angle depends on the length of time the field is on, τ, and its magnitude H_1

$$\theta = \gamma_N \tau H_1 \qquad \textbf{Eq. 3-8}$$

where τ is assumed to be much smaller than T_1 and T_2 (see below). A $\pi/2$ pulse is one which rotates the nuclear magnetization vector clockwise by $\pi/2$ radians about the $x^{'}$ axis, down to the $y^{'}$ axis; while in the laboratory frame, the equilibrium nuclear magnetization spirals down around the z axis to the *xy* plane. One can see why the rotating frame of reference is helpful in describing the behavior of the nuclear magnetization in response to a pulsed magnetic field. Similarly a π pulse will rotate the nuclear magnetization vector by π radians. If the nuclear magnetization was initially along the *z* (*x* or *y*) axis it is rotated into the $-z$ ($-x$ or $-y$) axis.

3.4.1 Echo and the spin-spin relaxation time T_2

The spin-spin relaxation time T_2 is the time scale of the dephasing of the transverse nuclear magnetization. It is characterized by the defocusing of nuclear magnetization during the pulse sequence and is determined by the decay of the echo intensity (see below) as a function of the interval between pulses. A π/2 pulse is first applied to the spin system which rotates the nuclear magnetization down into the *x'y'* plane (in the rotating frame). The transverse nuclear magnetization begins to dephase. At some point in time (τ) after the π /2 pulse, a π pulse is applied. This pulse rotates the nuclear magnetization by π about the *x*' axis. The π pulse causes the nuclear magnetization to rephase at least partially and to produce a signal called an echo. We determine T_2 by varying the time τ between the π /2 pulse and the π pulse, and measuring the exponential decrease of the echo. The maximal value of the signal as a function of τ behaves according to:

Eq. 3-9 $$Echo(\tau) = Echo(0) \cdot e^{\frac{-\tau}{T_2}}$$

3.4.2 The saturation recovery and the spin lattice relaxation T_1

In order to study spin dynamics of Fe8, nuclear spin-lattice relaxation times T_1 was measured using pulsed spin-echo techniques. In the measurements of T_1, the saturation-recovery method was used. Figure 3-9 shows the scheme of the pulse sequence. The intensity of the spin echo is measured as a function of delay time t after the comb (saturation) pulses. Generally, the magnetization of $I = 1/2$ nuclear spins, such as protons, recovers exponentially after the saturation with a time constant T_1. Then, T_1 is determined by a fitting of the following equation:

Eq. 3-10 $$Echo(t) = Echo(\infty)\left[1 - \exp\left(\frac{-t}{T_1}\right)\right]$$

were M(t) denotes a nuclear magnetization at delay time t. During the T_1 measurements, of course, t is varied but τ is fixed. In principle, T_1 characterizes the time scale of the energy transfer to the reservoir (lattice) caused owing to the nuclear relaxation.

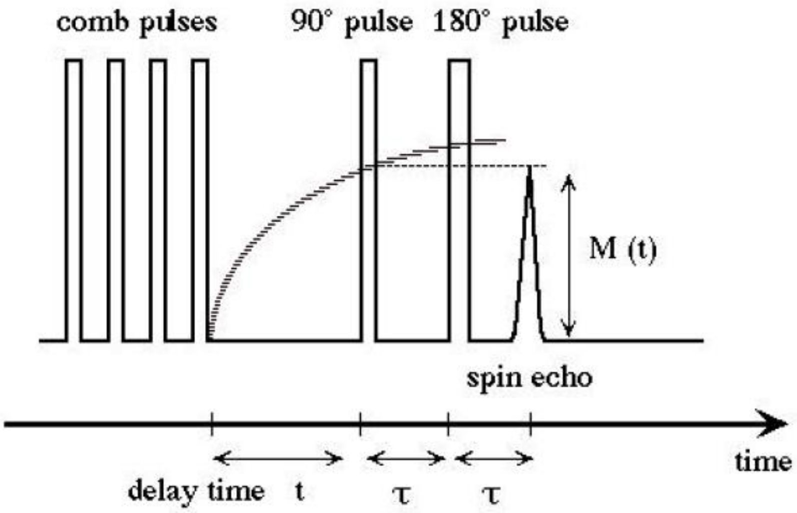

Figure 3-9: A scheme of NMR pulse sequence for the measurement of T_1. The nuclear magnetization along the applied field (shown as dashed curve) is recovered after saturation pulses. The spin echo is formed at the time t after the 180° pulse, where t denotes the time between 90° pulse and 180° pulse.

3.4.2 Field sweep

The NMR spectrum (or line shape) reflects the spectrum of frequency absorption of the studied nuclei, from which one can study the magnetic environment and interactions in the vicinity of the nuclei. When the spectrum is broader than the bandwidth of the receiver one has to sweep the external magnetic field. By doing that one puts different groups of the nuclei in resonance, and scans the different sections of the NMR spectrum. The full spectrum is reconstructed by time integrating over different signals obtained for the different fields. Each integral corresponds to the intensity of the spectrum at the corresponding frequency.

Chapter 4

Experimental results

4.1 Magnetization measurements

The purpose of this experiment was to see the staircase shape of the magnetization of Fe8, as a proof of its macroscopic quantum nature, and also to try out an experiment that will examine the influence of RF on the hysteresis loop.

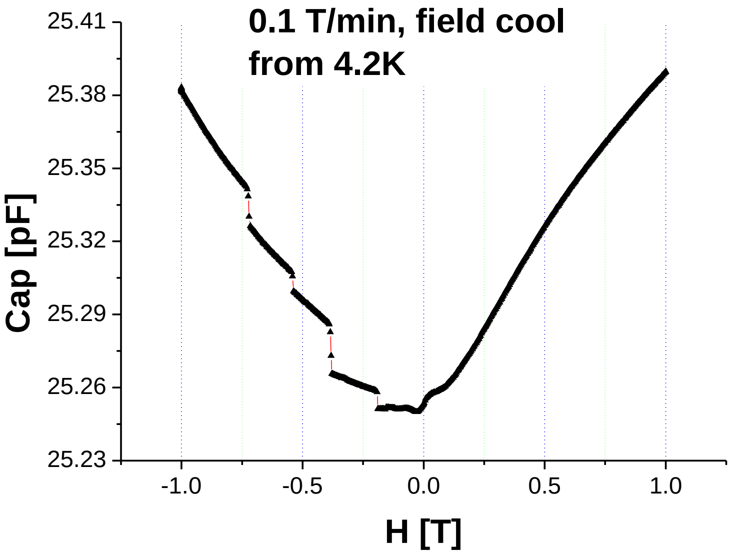

Figure 4-1: Capacitance Vs. Magnetic field at base temperature. The slope in the positive magnetic field is due to the gradient from the external field. The clear steps indicates the jumps in the magnetization.

The magnetization of the sample was measured in two configurations – first the sample was cooled down to $T \approx 40mK$ to examine the molecule in the pure quantum tunneling regime (which is <400mK) but with different sweeping rates of the magnetic field; Second, the sweeping rate was constant but the measurements were taken at different temperatures. In every measurement we first applied a field of +1 T and waited until thermal equilibrium is reached. We then record the capacitance, temperature, and field values, as the field is swept from +1 T to -1 T. In Figure 4-1 we show one complete measurement of the capacitance vs. the magnetic field. When the field is positive the capacitance is a smooth function of the field. This is because the spins are at their ground state for all positive fields and have nowhere to tunnel to. In principle, C should have been constant for $H>0$ since the magnetization is constant. However, in a DR it is difficult to place the sample in the center of the main magnet, and the gradient has some field dependence. The measurements at $H>0$ could be used to calibrate the field gradient. Once the field becomes negative, clear jumps in the capacitance are observed, indicating jumps in the magnetization that are taking place as the magnetization is tunnels between the states.

In Figure 4-2 the capacitance vs. the magnetic field is presented at eight different sweeping rates. There are clearly four steps at sweeping rates 0.1 - 0.3 T/min that become smaller as the sweeping rate is increased, until only the step at ~0.22T is seen.

In the second part of this experiment, we kept the sweeping rate constant (0.5 T/min) but lowered the temperature (Figure 4-3). When the temperature is higher, the steps get smaller and less sharp until they vanish. These measurements were taken during the cooling process, so the temperature of the sample is higher than the temperature of the thermometer.

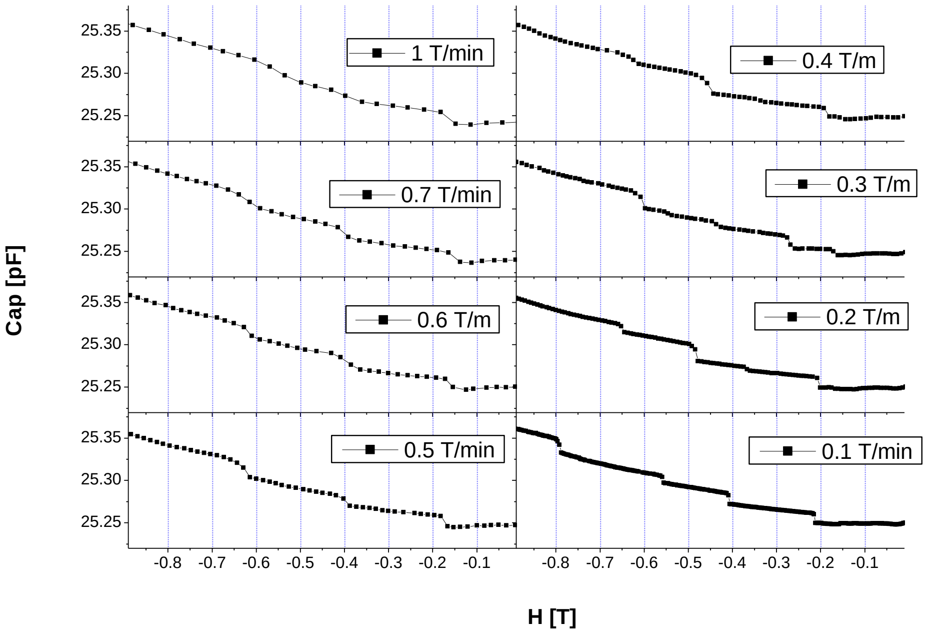

Figure 4-2: Capacitance Vs. Magnetic field at base temperature with different sweep rates.

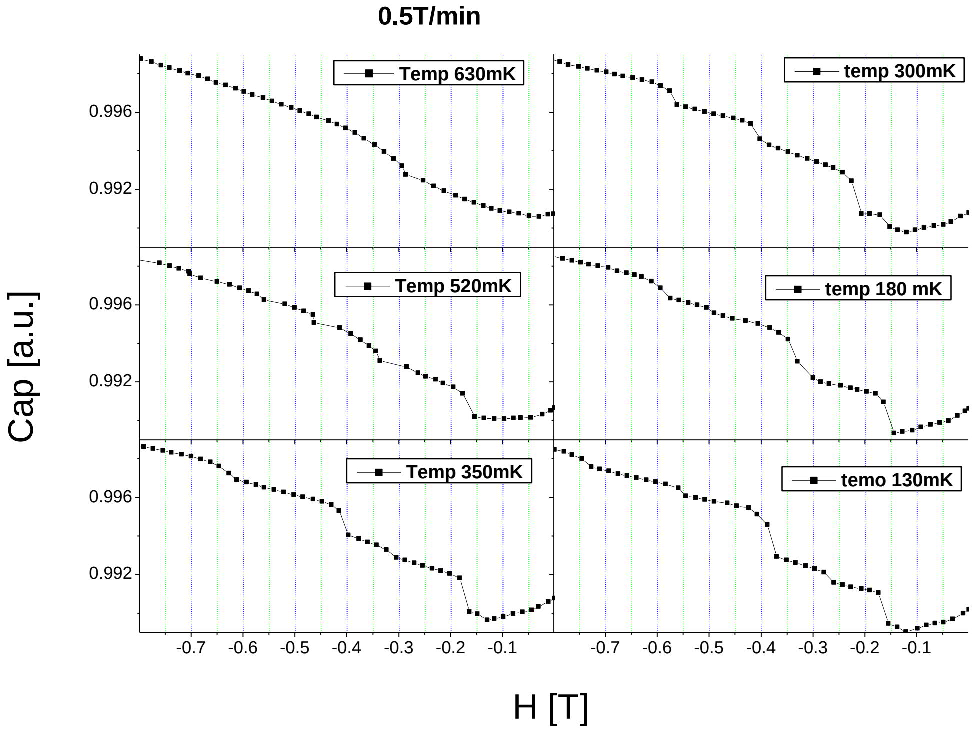

Figure 4-3: Capacitance vs. Magnetic field with sweep rate of 0.5T/min at different temperatures. The indicating temperature is of the mixing chamber, so the temperature of the sample is higher.

4.2 ^{1}H NMR Measurements

Due to the line broadening (Figure 2-5), the experimental set up and the long T_1 of Fe8 (Figure 2-4), it is hard to detect its signal. The GE-varnish, however, has a narrow line with a shorter T_1. We confirm the presence of RF using its signal. Because we use a split coil (there is a "hole" in the middle for the sample holder) the system is not optimized for detecting the signal. Moreover, due to technical difficulties, our RF transmitter and detector are in different rooms, and the long line between the coil and the rest of the system causes attenuation of the signal.

We measured the Echo intensity as a function of field and pulse width (Figure 4-4). We found out that the full width at half maximum is 0.004±0.0005T, which means that the protons experience a variation in the magnetic field of this value. When we looked for the ideal pulse width (Maximum echo) we found it to be 1.5±0.5μsec. From $\omega = \gamma H$, we calculated H_1 to be 0.024±0.004T.

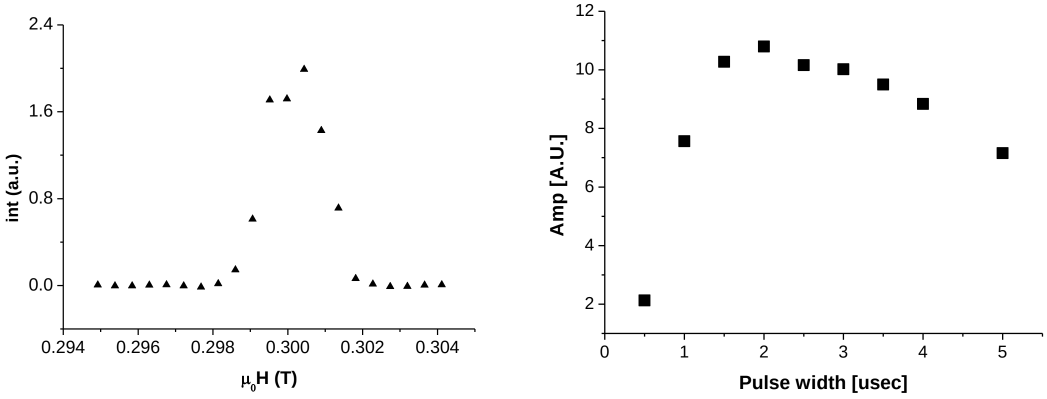

Figure 4-4: Echo intensity as a function of field (right) and pulse width (left).

Nuclear spin-spin relaxation time T_2 was measured using pulsed spin-echo techniques (see section 3.4). The echo intensity as a function of τ (the time between the π/2 pulse and the π pulse) was measured in several temperatures (Figure 4-5).

We also measured T_1 at base temperatures in 0.3T (12.71MHz), as one can see in Figure 4-6, using the pulse sequence in Figure 3-9. The T_1 was 92±13 sec, much shorter than Ueda's results (Figure 2-3). After measuring only GE-varnish in our NMR system (not in the DR) we confirmed that this T_1 came from the varnish and not from the sample (Fe8).

To summarize, we see an NMR signal from the Varnish, but the transmitted RF is felt also by the sample. The magnetic field H_1 of the RF coil is 0.024±0.004T.

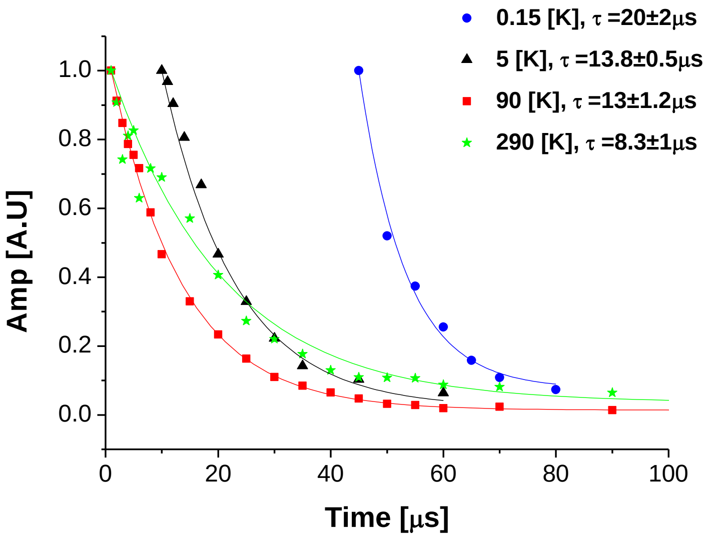

Figure 4-5: T_2 measurements for several temperatures.

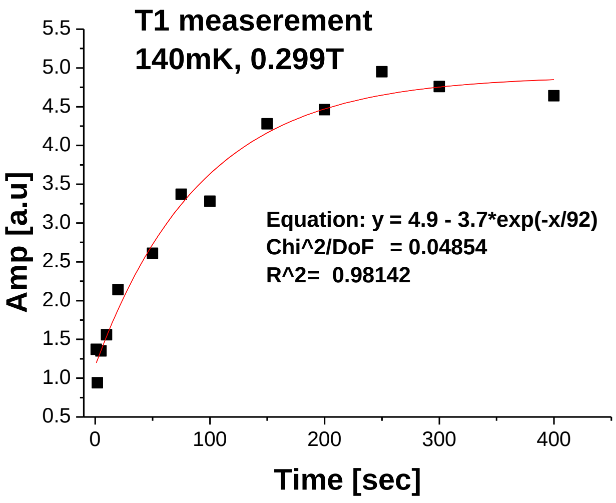

Figure 4-6: T_1 measurements for base temperature.

4.3 Magnetization Measurements with RF

After seeing clear steps in the magnetization and detecting the ^{1}H nuclei, we combined the two techniques to see the influence of the RF on the steps in the magnetization curve. For technical reasons we could transmit only above 10.7MHz, so we decided to transmit at a field of 0.3T (12.71MHz).The scheme of the measurements with RF is presented in Figure 4-7. We sweep the magnetic field from positive to negative, and stop for several seconds to transmit the RF at 0.3T (we do it at the positive side of the magnetic field to avoid transition of the molecule spin due to heating). One can see that the temperature rise due to the transmitting of RF is low, and the first two jumps takes place in the time regime of the T_1(which is longer than 1000 sec). One can also see jumps in the temperature in the negative field regime which will be discussed later. To make the measurement with and without RF as similar as we can, we stopped in both cases at a field of 0.3T for several seconds.

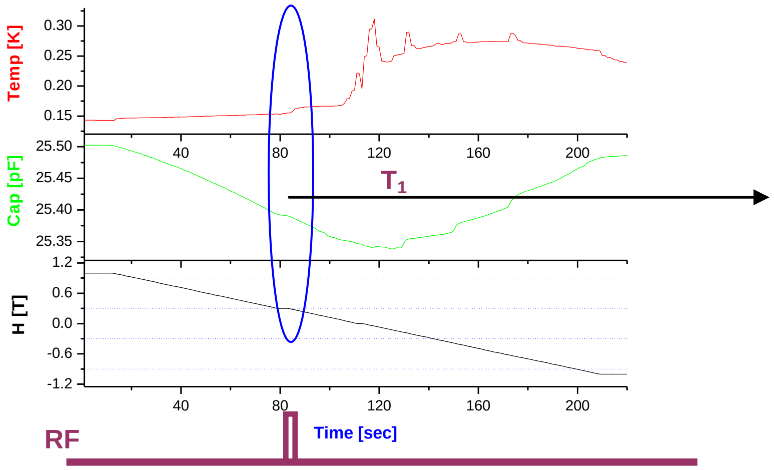

Figure 4-7: scheme of the measurements with RF. We sweep the magnetic field from positive to negative, and stop for several seconds to transmit the RF at 0.3T. We see that the temperature rise due to the transmitting is low, and the first two jumps are in the regime of the T_1.

We can estimate the nuclear temperature (T_n) to be:

Eq. 4-1
$$\frac{\omega}{k_B T_{el}}\left(1-\exp\left(\frac{t}{T_1}\right)\right)=\frac{\omega}{k_B T_n}\xrightarrow{\sim 100s} T_n=\frac{T_{el}}{1-e^{-0.1}}\sim 10T_{el}$$

where T_{el} is the electron temperature (~150mK), t is time and ω is the RF frequency. When we apply a comb of pulses, the nuclei lose their orientation, as if their temperature is very high. After 100 sec, the nuclear temperature goes down, but it is still 10 times more than the electrons (the temperature goes from ~150mK$_{(t=0)}$ before the RF pulses to ~1.5K$_{(t=100)}$ when the jumps occur).

The results are summarized in Figure 4-8. We did several measurements with and without RF, and looked for an effect on the position or size of the jumps. Although we raised the temperature of the nuclei to ~1.5k, therefore changed their T_2 by an order of magnitude (see Figure 2-4), we saw no effect on the magnetization jumps.

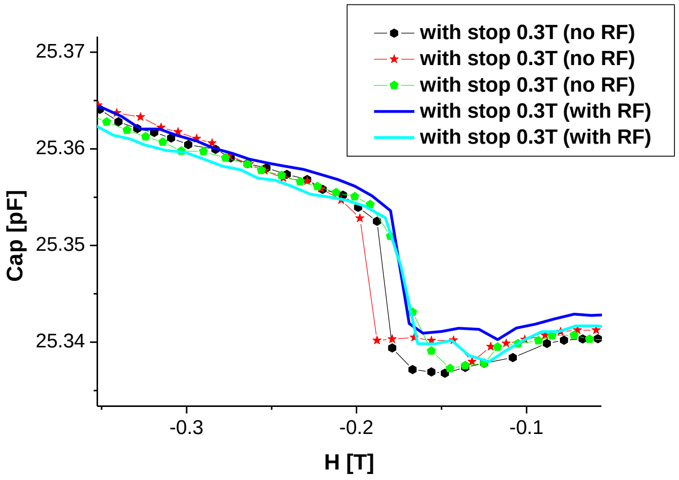

Figure 4-8: Capacitance (=Magnetization) measurement with and without RF. We saturate the nuclei and see no effect.

4.4 Electromagnetic radiation

The capacitance vs. the applied magnetic field (and time) is shown again in Figure 4-9(a). In Figure 4-9(b) we focus on the temperature reading of the thermometer compared to C. For positive field the temperature is quite stable. At zero field there is a big and broad increase in the temperature. The rise in the temperature at zero field is caused by an eddy currents developing in the copper wires and by the change in the sweep rate during the transition from positive to negative field. At negative fields there is a mild decline in the temperature, accompanied by clear temperature spikes.

A simple approach to the data analysis is to present $(2/\Delta C)dC/d\mu_0 H = (1/M_0)dM/d\mu_0 H$ where ΔC is the difference in capacitance between H=0 and H=1T, and M_0 is the saturation magnetization. This quantity is significant only at the jumps. We also subtracted from *T* a polynomial fit to the mild temperature decline for negative fields. The resulting $(1/M_0)dM/d\mu_0 H$ and ΔT are shown in Figure 4-10. It is now clear that the thermal spikes of a few tens of mili-Kelvin occur less about 3 sec after the capacitance (magnetization) jumps, and that every magnetization jump is accompanied by a thermal spike. The thermal spikes begin at the lowest field where tunneling is taking place, indicating that they involve transitions between the lowest-lying states of the molecular spin.

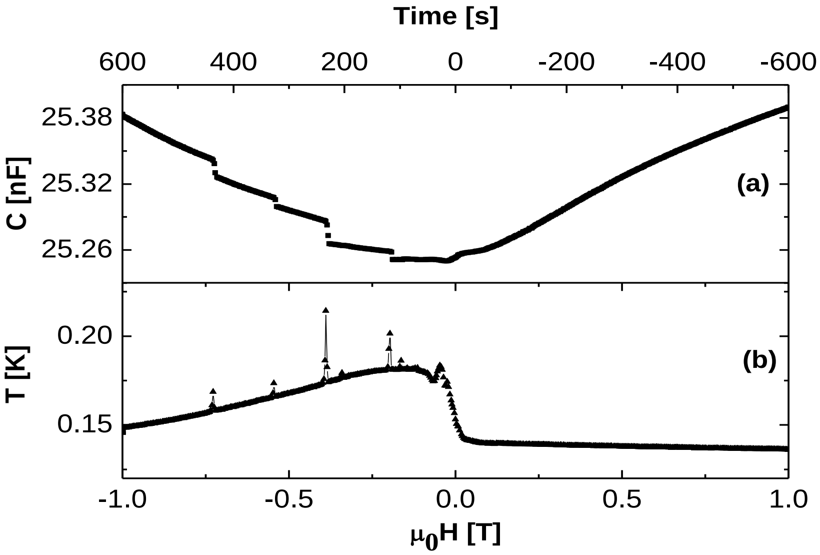

Figure 4-9: (a) capacitance (which represents magnetization) and (b) temperature vs. magnetic field swept from positive to negative. Steps in the capacitance indicate QTM in the sample. Spikes in the temperature indicate energy bursts.

A priori, there could be many reasons for the thermal spikes. The first that comes to mind is heating from the moving part of the capacitor. To disqualify this possibility we jammed the movable capacitor plate by raising the lower plate until the plates touch each other, and repeated the measurement. The results are presented in Figure 4-11(a-b). Because the capacitors' plates were jammed, there is no change in the capacitance, but the spikes in the temperature are still present.

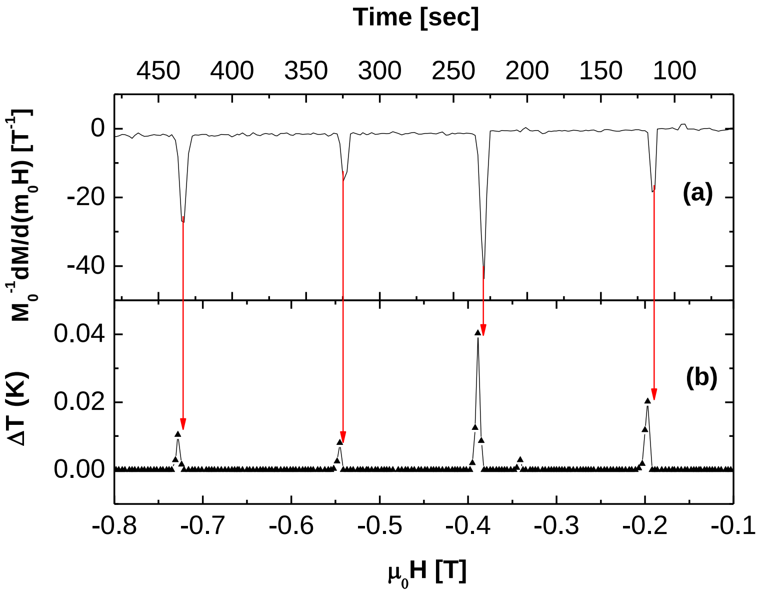

Figure 4-10: (a) Normalized derivative of the magnetization extracted from the capacitance (see text) and (b) temperature spikes vs. magnetic field swept from positive to negative. The changes in the magnetization are followed by an increase in the temperature, indicating release of energy.

Another source of heating could be phonons. Since the entire system is in vacuum, the energy could reach the thermometer only via the copper wire thermal link. To check this possibility we performed two experiments. First, we moved the thermometer to a separate copper wire, thermally linked directly to the mixing chamber, but not to the sample. We confirmed that the results presented in Figure 4-9 are reproducible in this configuration (not shown). Second, we blocked the line of sight between sample and thermometer by covering the sample with a copper cylinder. The results are depicted in Figure 4-11(c-d). The steps in the capacitance are still seen, although not all of them and they are somewhat broader for a reason that is not clear to us. Perhaps the force acting on the sample causes it to fracture after many field cycles. In contrast, the jumps in the temperature disappeared completely. The last two experiments confirmed that the cause of the temperature spikes is electro-magnetic radiation and not phonons.

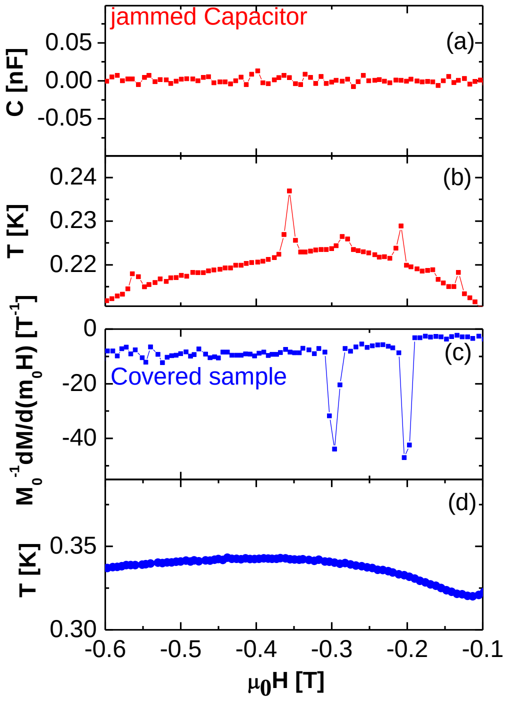

Figure 4-11: Test cases: The capacitance (a) and temperature (b) vs. magnetic field swept from positive to negative with jammed capacitor. The rise in the temperature indicates the change in the magnetization. The normalized derivative of the magnetization (c) and temperature (d) vs. magnetic field (same sweeping direction) with covered sample. The change in the magnetization is not followed this time by an increase in the temperature.

Next we identified the energy levels that participate in the transitions. The main part of the Hamiltonian is given by Eq. 1-10. The energy as a function of field and corresponding level quantum number *m* is shown in Figure 1-2. In the inset, a zoom view of the avoided level crossing taking place at $\mu_0 H$=-0.4 T is presented. There are two possible transitions. The first possibility is that the photon is emitted by transition between the avoided levels as indicated by the vertical arrow in the inset of Figure 1-2. The photon energy in this case equals that of the tunnel splitting which is ~10^{-6} K [12]. The second possibility is that photons are emitted due to transition between states with the same sign of their quantum number *m* as indicated by the solid arrows in the main panel of Figure 1-2[56, 61]. In the case of Mn_{12} these were high-lying thermally excited states such as *m=1* to *m=2*. In the experiment presented here these must be low-lying states. In this case the photon energy is ~1 K. The difference in photon energy expected from these two possibilities is huge and can easily be distinguished.

To determine the energy released by the sample we have to convert the size of the thermal spikes to the energy detected by the resistor. For this purpose, we measured the energy needed to change the temperature of the thermometer by the same amount as in Figure 4-10, when the energy is injected directly into it. The temperature is determined by four-wire resistance measurement, with very low current of 0.7μA. Changing the current to 10μA for ~0.5sec and immediately after measuring it with 0.7μA produced a spike similar to the ones shown in Figure 4-10. The energy needed to produce these thermal spikes is ~0.25μJ.

Chapter 5

Simulation of QTM with stochastic field

QTM in magnetic molecules (MM) with high spin value is usually explained with the model of Landau and Zener (LZ). This theory predicts transition probabilities; however, it has not been able to account for the size of the magnetization jumps in molecular magnets. As we mentioned before, the discrepancy between Δ deduced from LZ experiments [12] and the one calculated from spectroscopic data is more than two orders of magnitudes [42]. The SS theory [43] takes into account the dephasing effect due to stochastic field fluctuations. In this section I will show some simulation results and will compare them to theoretical calculations.

5.1 Results with stochastic field, B(t) || z

We consider the simplest case where we add to Eq. 1-14 a magnetic field fluctuates in the *z* direction, namely, the Hamiltonian is:

Eq. 5-1 $$\mathcal{H}_0 = \left(\alpha t + B(t)\right) S_z + \Delta S_x$$

where *B*(*t*) is the stochastic field (We include $2\mu_B$ in the definition of *B*, where 2 is the g-factor). $S_x = 2\sigma_x$ and $S_z = 2\sigma_z$, where σ_x and σ_z are the Pauli matrixes. Now the Schrödinger equation is:

Eq. 5-2 $$i\hbar \frac{\partial}{\partial t}\left|n\right\rangle = \left[\alpha t S_z + \Delta S_x + \mathrm{B(t)} \cdot \mathrm{S_z}\right]\left|n\right\rangle$$

and it could be written in a dimensionless form as

Eq. 5-3 $$i\hbar\frac{\partial}{\partial t}\left|n\right\rangle=\left[\frac{\alpha}{\Delta}tS_z+S_x+\frac{1}{\Delta}\mathrm{B(t)}\cdot\mathrm{S_z}\right]\left|n\right\rangle$$

which with a bit manipulation is:

Eq. 5-4 $$i\frac{t_T}{t_z}\frac{\partial}{\partial(t/t_z)}\left|n\right\rangle=\left[\frac{t}{t_z}S_z+S_x+\frac{t}{\hbar}\mathrm{B(t)}\cdot\mathrm{S}\right]\left|n\right\rangle$$

where $t_T\equiv\hbar/\Delta$ is tunneling time, $t_z\equiv\Delta/\alpha$ is Zener time (in the adiabatic limit, γ ,which is t_Z/t_T, is much smaller than 1).

As we said before, B(t) is a flickering magnetic field (in the simulation $\mathrm{B}(t)\equiv\pm\mathrm{B}_0\hat{z}$), which means that B(t) has two values. The time interval between consecutive field changes is set randomly from an exponential distribution with a time scale τ_c (correlation time), such as:

Eq. 5-5 $$f(t\,|\,\tau_c)=\frac{1}{\tau_c}e^{\frac{t}{\tau_c}}$$

Or in dimensionless form:

Eq. 5-6 $$f\left(t\,|\left(\tau_c/t_z\right)\right)=\frac{1}{\tau_c/t_z}e^{\frac{t}{\tau_c/t_z}}$$

Using the definition of dephasing time $\tau_\varphi\equiv\dfrac{\hbar^2}{B^2\tau_c}$, and recalling that B has only two values, the Schrödinger equation can turn into:

Eq. 5-7 $$i\frac{t_T}{t_z}\frac{\partial}{\partial(x)}\left|n\right\rangle=\left[xS_z+S_x+\frac{t_T}{\sqrt{\tau_c\tau_\varphi}}\mathrm{A}(x)\cdot\mathrm{S}\right]\left|n\right\rangle$$

Where $x\equiv t/t_z$ and the correlator is given by:

Eq. 5-8 $$\left\langle\mathrm{A}(x)\mathrm{A}(0)\right\rangle=\exp\left(-x/\left(\tau_c/t_z\right)\right).$$

In Figure 5-1 we show result for various parameters of the time scale. We have some analytical results for several cases. In the adiabatic limit (graph (a) and (b) in this figure) one can see that for different dephase time we get different transitions and different final probability. When the dephase time and the correlation time are small, the results can be estimated to be $P=\left[1+0.4*\exp(-\pi/\lambda)\right]/2$[44], and because $\exp(-\pi/\lambda)$ is very small, one gets P=0.5 (the number 0.4 in the formula is due to a different notation). In the sudden limit (graph (c) and (d)) one can see that for different dephase time we get different transitions but almost the same final probability. For the simplest case where the correlation time is small, we can use Eq. 1-18, which one can see the result of the calculation and of the simulation in the section were $\gamma=10$ and $t_c/t_z=0.1$ (graph (d)).

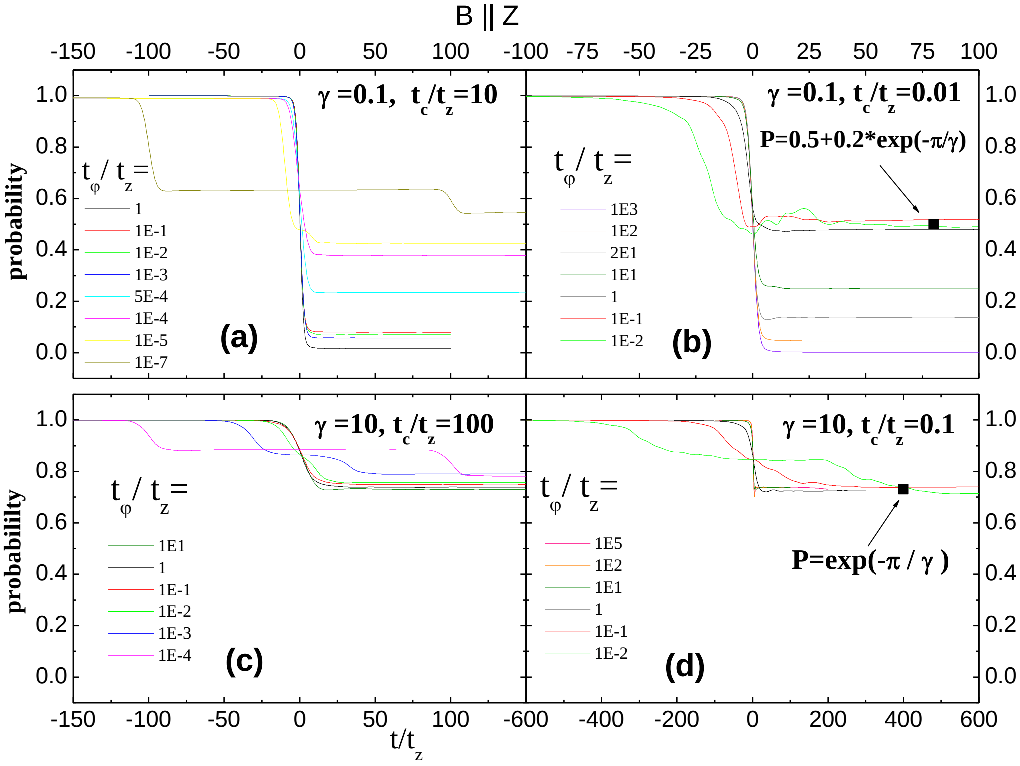

Figure 5-1: Simulation results for various parameters with B(t) || z. the black points are analytical calculations.

Chapter 6

Discussion and summary

6.1 Magnetization and RF

We raised the temperature of 10% of the nuclei from ~150mK to ~1.5k, therefore we changed their T_2 by an order of magnitude (see Figure 2-4). As we showed in section 1.5, the Shimshoni and Stern theory investigates the LZ model with dephasing effect due to stochastic field fluctuations, and gives a correction to the LZ model. In our experiment, we don't know if we fulfill the SS conditions, but as one can see in Eq. 1-23, changing T_2 by one order of magnitude should influence the probability strongly (T_2 is in the exponent), hence should change the height of the steps. Nevertheless, the RF had no effect on the jumps.

Looking at our simulation results (Figure 5-1 (c)+(d)), one can see that when $\gamma = 10$, the probability is independent of τ_φ or τ_c (which means that the probability is independent on the magnitude or the correlation time ("T_2") of the fluctuating field). An optional explanation is that in our experiment γ>>1. γ can be written as $\hbar\alpha / \Delta^2$, which mean that maybe Δ should be smaller than $5 \cdot 10^{-6}$, which is suitable for both cases (theoretically and experimentally).

6.2 Electromagnetic radiation and Super Radiance

Molecular Magnets can be used as a radiation source in the regime of micro and sub-millimeter wavelength: the quantum nature of the molecule implies that at low temperature and varying magnetic field, the electrons change their energy state, which means that they can emit or absorb photons. Experiments with micro-wave radiation have been carried out on Fe8 (radiation from external source) in which the absorption and the connection to the magnetization curve was investigated [45-51]. Some theoretical works [52-55] have proposed that single-molecule magnets could be used to generate superradiance (SR). Tejada *et al.* reported that during magnetization avalanches of the molecular magnet Mn12 acetate millimetr-wave radiation was released [56, 57], and also registered it as a patent [58]. Moreover, in the same year, Bal et al published an experimental upper bound on superradiance emission from Mn12 acetate [59], but as far as we know, no attempt has been made to measure the radiance from Fe8.

We found energy bursts each time the molecule undergoes a magnetization jump, confirming their quantum nature. A series of tests indicated that photons carry out the energy.

A question that should be asked is how come this phenomenon has not been seen before. We believe that all the experiments with Fe_8 used exchange gas or liquid as a cooler, and not a thermal link. In the former case, the radiation emitted from the sample is hard to detect. Moreover, most experiments have been done with small crystals to prevent avalanches, so the radiation was weak.

To estimate this energy theoretically we consider the possibility where by sweeping the field from positive to negative, the tunneling that is taking place at $\mu_0H=-0.4$ T is from m=-10 to m=8, followed by a transition from m=8 to m=9 to m=10. Judging from the relative area of the magnetization derivative peaks in Figure 4-10, about 0.4 of the total spins tunnel at this crossing. The expected energy release after the tunneling is twice ~5 K (see Figure 1-2) or

1.4×10^{-22} J. The 20mm^3 sample, with ~2nm^3 unit cells [22], has 10^{19} molecules. Therefore, the energy that was released is 0.6 mJ. Considering the distance between sample and thermometer and its cross-section, the solid angle of the thermometer is 0.02±0.004. Therefore, the energy that should reach it is 12μJ. This is much closer to the estimated value (~0.25μJ) than an avoided levels photon of 10^{-6} K. Therefore, it is clear that photons emitted by transitions between low lying states, and not avoided levels, are responsible for the thermal spikes.

Having established the energy carrier and the energy source we examine first the possibility of black body radiation. The temperature of the sample can increase after the magnetization steps but not too much since we see the consecutive step. An upper limit is 5 K where steps are no longer observed. At this temperature Stephan-Boltzmann law would predict a radiation power two-three order of magnitude smaller than what is needed to produce our temperature spikes.

Next we examine the possibility of SR. The most important condition for SR is $\lambda > l$ [62], where λ is the photon wave length and l the sample size ~2.7mm in our case. λ for a 5 K photon is 3 mm. Therefore, this SR condition is obeyed.

The second condition is that the transition rate will be bigger than any other decoherence rate of the molecular spins. The transition rate for a single molecule emitting a photon is [56]

Eq. 6-1
$$\Gamma_1 = \frac{2g^2\mu_B^2}{3\hbar^4c^3}(S-m)(S+m+1)(E_m-E_{m+1})^3.$$

For the *m=8* to *m=9* this gives $\Gamma_1 = 10^{-7}$ sec^{-1}. In the SR case the minimal transition rate $\Gamma_{SR} = N\Gamma_1$, where *N* is the total number of molecules in the *m=8* (without the thermal factor which exists in Mn$_{12}$). The maximum transition rate is $\Gamma_{SR} = N^4\Gamma_1/4$ [62]. This gives $\Gamma_{SR} > 10^{11}$ sec^{-1}. Since there is no temperature dependence of the tunneling in Fe$_8$ below 400mK it is believed that the source of dephasing is nuclear moments, and it is given by

$\Gamma_{nuclear} \sim 10^8$ sec^{-1} [63]. Therefore, the second SR condition $\Gamma_{SR} \gg \Gamma_{nuclear}$ is also obeyed. Thus, it is conceivable that the transitions between low-lying states in Fe$_8$ are accompanied by SR of photons.

Finally, we consider the possibility of classical magnetic dipole radiation. It was shown in ref [52] that since this radiation is a collective phenomenon that conserves the total spin value, it is equivalent to SR, provided that the relaxation between levels occurs fast enough. Eq. 18 in Ref [52] relates the emitted power I to the second derivative of the magnetization projection by $I = \frac{2}{3c^3}\left(\frac{d^2 m_z}{dt^2}\right)^2$, which could be approximated as $\frac{2}{3c^3}\frac{\Delta m_z^{\ 2}}{\Delta t^4}$. Using this relation, our energy burst for the transition between say $m=8$ to $m=10$ can be viewed as dipole radiating classically for ~10 nsec. This time is much shorter than $1/\Gamma_1$ and closer to $1/\Gamma_{SR}$, hence the equivalence to SR.

References

1. C . Sangregorio, T. Ohm, C. Paulsen, R. Sessoli, D. Gatteschi, Phys. Rev. Lett., 78 4645 (1997).

2. A. -L. Barra, P. Debrunner, D. Gatteschi, Ch. E. Schulz and R. Sessoli, Euro. Phys. Lett. 35 134 (1996).

3. Tejada, J., Chudnovsky, E. M., Barco, E., Hernandez J., M. Spiller, T. P. *Nanotechnology* 12, 181 (2001).

4. Leuenberger, M. N., Loss, D. *Nature* (London) 410, 789 (2001).

5. Shafir, O. et al. *Phys. Rev. B* 72, 092410 (2005).

6. Bogani, L., Wernsdorfer, W. *Nature Materials* 7, 179 (2008).

7. Cage, B. et al. *Polyhedron*. 26, 2413 (2007).

8. D. Gatteschi, R. Sessoli and J. Villain, Molecular Nanomagnets, Oxford University Press, Oxford (2006).

9. D. Gatteschi, R. Sessoli, Angew. Chem. Int. Ed. 42, 268 (2003),.

10. J. Villain, A. Fort, J. Euro. Phys. B. 17, 69 (2000).

11. R. Caciuffo, G. Amoretti, A. Murani, R. Sessoli, A. Caneschi, D. Gatteschi, Phys. Rev. Lett., 81(21), 4744 (1998); Yves Pontillon, A. Caneschi, D. Gatteschi, R. Sessoli, E. Ressouche, J. Schweizer, E. Lelievre-Berna, J. Am. Chem. Soc. 121, 5342 (1999).

12. W . Wernsdorfer, R. Sessoli, A. Caneschi, D. Gatteschi, A. Cornia, D. Mailly, J. Appl. Phys. 87, 5481 (2000).

13. E.M. Chudnovsky, D.A. Garanin, Phys. Rev. Lett., 87, 187203 (2001).

14. C. Zenner. Proc. Roy. Soc. London A, 137, 696 (1932).

15. L. Landau, Phys. Z. Sowjetunion. 2, 46 (1932).

16. E.C.G. Stückelberg, Helv. Phys. Acta. 5, 369 (1932).

17. K. Mullen, E. Ben-Jacon, Y. Gefen, and Z. Schuss, Phys. Rev. Lett. 62, 2543 (1989).

18. F . Hartmann-Boutron, P. Politi, J. Villain, Int. J. Mod. Phys. B, 10, 2577 (1996).

19. N . V. Prokof'ev, P. C. E. Stamp, Phys. Rev. Lett. 80, 5794 (1998).

20. N . V. Prokof'ev, P. C. E. Stamp, J. Low Temp. Phys. 104, 143 (1996).

21. W . Wernsdorfer, T. Ohm, C. Sangregorio, R. Sessoli, D. Mailly, C. Paulsen, Phys. Rev. Let. 82, 3903 (1999).

22. K. Wieghardt, K. Pohl, I. Jibril and G. Huttner, Angew. Chem. Int. Ed. Engl. 23, 77 (1984).

23. C. Delfs, D. Gatteschi, L. Pardi, R. Sessoli, K. Wieghardt and D. Hanke, Inorg. Chem. 32, 3099 (1993).

24. M. Ueda and S. Maegawa, J. Phys. Soc. Jpn. 70 (2001).

25. A. Caneschi, D. Gatteschi, C . Sangregorio, R. Sessoli, L. Sorce, A. Cornia, M.A. Novak, C. Paulsen, W, Wernsdorfer, JMMM, 200, 182 (1999).

26. W. Wernsdorfer, A. Caneschi, R. Sessoli, Phys. Rev Let. 84, 2965 (2000).

27. R. Sessoli, A. Caneschi, D, Gatteschi, L. Sorace, A. Cornia, W. Wernsdorfer, J. Magn. Magn. Mater 226 1954 (2001).

28. W. Wernsdorfer, A. Caneschi, R. Sessoli, Phys. Rev Letters, 84, 2965 (2000).

29. D . Gatteschi, A. Lascialfari, F. Borsa, J. Magn. Magn. Mater. 185, 238 (1998).

30. Y . Furukawa, K. Kumagai, A. Lascialfari, S. Aldrovandi, F. Borsa, R. Sessoli, D. Gatteschi, Phys. Rev. B, 64, 094439 (2001).

31. Y . Furukawa, K. Aizawa, K. Kumagai, A. Lascialfari, F. Borsa, J. Magn. Magn. Mater, 272, 1013 (2004).

32. Y. Furukawa, K. Aizawa, K. Kumagai, R. Ullu, A. Lascialfari, F. Borsa, J. Appl. Phys. 93, 107813 (2003).

33. Y. Furukawa, S. Kawakami, K. Aizawa, K. Kumagai, F. Borsa, Polyhedron 22, 2277 (2003).

34. M. Ueda, PhD thesis, Kyoto University, 2001.

35. M. Ueda, S. Maegawa, S. Kitagawa, Phys. Rev. B. 66, 073309 (2001).

36. K. Wieghardt, K. Pohl and W. Gebert, Angew. Chem. Int. Ed. Engl. 22, 722 (1983).

37. T. Sakakibara, H. Mitamura, T. Tayama and H. Amitsuka, Jpn. J. Appl. Phys. 37 5067 (1994).

38. H. Zijlstra, "Experimental methods in magnetism", North Holland Publishing Company,

39. A. G. Swanson, Y. P. Ma, J. S. Brooks, R. M. Markiewicz, N. Miura, Rev. Sci. Instrum., 61 (2), 848 (1990).

40. H. London, G.R. Clarke, E. Mendoza, Phys. Rev. 128, 1992 (1962).

41. "Partical Cryogenics – An introduction to labratory cryogenics", Oxford Instruments, (1996).

42. S. Carretta, E. Liviotti, N. Magnani, P. Santini, and G. Amoretti, Phys. Rev. Lett. 92, 207205 (2004).

43. E. Shimshoni and A. Stern, Phys. Rev. B 47, 9523 (1993).

44. Y. Kayanuma, J. Phys. Soc. Jpn. 53, 108 (1984).

45. M. Bal, Jonathan R. Friedman, Y. Suzuki, E. M. Rumberger, D. N. Hendrickson, N. Avraham, Y. Myasoedov, H. Shtrikman and E. Zeldov, Europhys. Lett. 71, 110 (2005).

46. M. Bal, Jonathan R. Friedman, W. Chen, M. T. Tuominen, C. C. Beedle, E. M. Rumberger and D. N. Hendrickson, cond-mat/0706.3471.

47. B. Cagea, S. E. Russek, D. Zipse, J. M. North, N. S. Dalal, Applied Physics Letters 87, 082501 (2005).

48. L. Sorace, W. Wernsdorfer, C. Thirion, A.-L. Barra, M. Pacchioni, D. Mailly, B. Barbara, Physical Review B 68, 220407 (2003).

49. K. Petukhov, W. Wernsdorfer, A.-L. Barra, and V. Mosser, Phys. Rev. B 72, 052401 (2005).

50. M. Bal and Jonathan R. Friedman, E. M. Rumberger, S. Shah, and D. N. Hendrickson, N. Avraham, Y. Myasoedov, H. Shtrikman, and E. Zeldov, Journal of Applied Physics, 99, 08D103 (2006).

51. K. Petukhov, S. Bahr, W. Wernsdorfer, A.-L. Barra, and V. Mosser, Phys. Rev. B 75, 064408 (2007).

52. E.M. Chudnovsky and D. A. Garanin, Physical Review Letters, Vo. 89, 157201 (2002).

53. V. I. Yukalov, Laser Phys. 12, 1089 (2002).

54. E. M. Chudnovsky and D. A. Garanin, Phys. Rev. Lett. 93, 257205 (2004).

55. V. K. Henner and I. V. Kaganov, Phys. Rev. B 68, 144420 (2003).

56. J. Tejada, E. M. Chudnovsky, J. M. Hernandez, and R. Amigó, Appl. Phys. Lett. 84, 2373 (2004).

57. Hern´andez-M´ınguez, M. Jordi, R. Amig´o, A. Garc´ıa-Santiago, J. M. Hernandez and J. Tejada, Europhys. Lett. 69, 270 (2005).

58. J. Tejada, J. M. Hernandez, R. Amigo, R.F. Ziolo, U.S. Pat. Appl. Publ. 15 (2004).

59. M. Bal, Jonathan R. Friedman, K. Mertes, W. Chen, E. M. Rumberger, D. N. Hendrickson, N. Avraham, Y. Myasoedov, H. Shtrikman and E. Zeldov, Physical Review B, 70, 140403(R) (2004).

60. Barra, A. -L., Debrunner, P., Gatteschi, D., Schulz, Ch. E., Sessoli, R. Superparamagnetic like behavior in an octanuclear iron cluster. Euro. Phys. Lett. 35, 133 (1996).

61. Bal, M. et al, Experimental upper bound on superradiance emission from Mn12 acetate. Phys. Rev. B 70, 140403 (2004).

62. Dick, R. H. Coherence in spontaneous radiation processes. Phys. Rev. 93, 99 (1954).

63. Keren, A. et al. Experimental estimates of dephasing time in molecular magnets. Phys. Rev. Lett. 98, 257204 (2007).

חקירת השפעת
הפלקטואציות הגרעיניות
על מנהור קוונטי מגנטי

אורן שפיר

חקירת השפעות הפלקטואציות הגרעיניות על מנהור קוונטי מגנטי

חיבור על מחקר

לשם מילוי חלקי של הדרישות לקבלת התואר דוקטור לפילוסופיה

אורן שפיר

הוגש לסנט הטכניון – מכון טכנולוגי לישראל

ניסן תשס"ט חיפה אפריל 2009

המחקר נעשה בהנחיית פרופ' עמית קרן בפקולטה לפיסיקה בטכניון.

אני מודה מקרב לב לפרופ. עמית קרן על הדרכתו המעולה, תמיכתו ועידודו לאורך כל התקופה.

אני מודה לפרופ. פולטורק ולפרופ. רזניקוב על עזרתם עם ה- DR. אני מעריך מאוד את עזרתם של דר. שינין, דר. קפון ופרופ. כפתורי בהכנת הדגמים ואפיונם. תודה גדולה לפרופ. מיאגאווה ודר. יואדה עבור הדגמים הראשונים ולדר. יואדה עבור עזרתה בכתיבת התיזה. עבור עזרה בהבנת המודל של לאנדאו וזנר תודתי נתונה לד"ר אפרת שימשוני.

הוקרה מיוחדת על עזרתם הגדולה של הטכנאים – גלינה, שמואל ודר. לאוניד אומין.

תודה לכל חברי בקבוצות המחקר מגנטיות וטמפרטורות נמוכות.

תודה מיוחדת לבלהה, זאת שעמדה לצידי ובזכותה התקופה הזו היתה יותר מסתם תקופת לימודים בעבורי.

אני מודה לטכניון על התמיכה הכספית בהשתלמותי.

תקציר

צברים של מגנטים מולקולריים המכילים יוני מתכת פאראמגנטיים, נמצאים במחקר נרחב כמודל למגנטיות בסקלה הננומטרית, במיוחד בגלל האפקטים הקוונטים כמו המנהור של המומנט המגנטי . המולקולה המגנטית $[(C_6H_{15}N_3)_6Fe_8O_2(OH)_{12}]Br_7(H_2O)Br\cdot 8H_2O$, או בקיצור Fe8, היא תרכובת מייצגת שבה התגלה מנהור קוונטי של המגנטיזציה (QTM), ועבודת מחקר זו מתרכזת בה.

שדה מחקר זה הפך למעניין יותר בגלל היישומים העתידיים של מולקולות אלו. הטכנולוגיה היום הגיעה לנקודה שבה ניתן להשפיע על אטום בודד או מולקולה בודדת , ובכך מאפשרת הקטנת יחידת הזיכרון המגנטי מהגודל הנוכחי של 10^8 אטומים לביט (יחידת זיכרון) [3], למולקולה בודדת. כמו כן ניתן למצוא עבודות המקשרות בין מגנטים מולקולריים למולטי-ביט, לספינטרוניקס ולשיפור הקונטרסט בהדמיה מגנטית גרעינית.

המולקולה Fe8 שייכת לקבוצה של מולקולות בעלות ספין גבוה. מולקולות אלה מסתדרות על שריג כאשר המרחק בין מולקולות שכנות גדול כך שבטמפרטורות הנמוכות מגודל האינטראקציה בין היונים בתוך המולקולה (J), המולקולות מתנהגות כמו ספינים גדולים בלי אינטראקציה ביניהן. כל מולקולה של Fe8 מכילה 8 יוני ברזל Fe^{+3} (בעלי ספין של 5/2), שהאינטראקציה בינם היא אנטיפרומגנטית. התכונות המגנטיות של המולקולה הוסברו ע"י מודל פשוט עם ספין כולל $S=10$ הבנוי משישה ספינים מקבילים אחד לשני והשניים הנותרים בכיוון אנטי- מקביל לשאר (מודל זה אומת במדידות של פיזור נויטרונים [8]). התוצאות הניסיוניות של מדידות מגנטיות בטמפרטורות נמוכות מראות אנאיזוטרופיה התלויה בכיוון השדה המגנטי ביחס לצירי הגביש.

כאשר למולקולה יש אנאיזוטרופיה מגנטית לאורך ציר z ניתן לרשום את המילטוניאן הספין של מולקולה בודדת בשדה מגנטי H_z בצורה:

$$\mathcal{H} = DS_z^2 + g\mu_B H_z S_z$$

כאשר D הוא הגודל המתאר את גודל האנאיזוטרופיה, S_z הוא רכיב הספין של המולקולה בכיוון z, $g = 2$, μ_B הוא קבוע המגנטון של בוהר , ו- $g\mu_B H_z S_z$ הוא איבר זימן . לכן ללא שדה מגנטי מצבי האנרגיה של ספין מעלה (בכיוון +z) וספין מטה (בכיוון -z) תהיה שווה . בטמפרטורות גבוהות (מעל לגודל האנאיזוטרופיה של המולקולה) הספין של המולקולה יכול להתהפך ממצב מעלה למצב מטה ולהיפך ע"י מעבר

תקציר

תרמי מעל למחסום האנאיזוטרופיה , אבל כאשר הטמפרטורה נמוכה בהרבה ממחסום זה , הערוץ היחידי האפשרי למעבר בין מצבי הספין הוא ע "י מנהור קוונטי . המינהור בין מצבי ספין שונים אפשרי כאשר בהמילטוניאן של הספין מופיע ביטוי נוסף שאינו מתחלף עם רכיב הספין S_z, במקרה שלנו $E \cdot \left(S_x^2 - S_y^2\right)$. התנהגות זו מעניינת כי היא מאפשרת לנו "לראות" תופעות קוונטיות ע"י מדידות מקרוסקופיות. זוהי התופעה הנקראת "מינהור קוונטי של המגנטיזציה.

המודל הפשוט ביותר מדבר על בור פוטנציאל כפול. אם פונקציות הגל של המצבים בבור חופפות, כלומר יש אינטראקציה בינהן, נוצר פיצול בין רמות האנרגיה המנוונות הנקרא "פיצול המינהור", ומסומן Δ_T. הסיכוי למנהור תלוי ביחס בין האנרגיה של פיצול המנהור לאנרגית המחסום בין הבורות . רמות האנרגיה המתאימות להמילטוניאן ניתנות לחישוב ע"י ליכסון המטריצה של 2S+1 המצבים האפשריים. התוצאות מראות שרמות האנרגיה בנוכחות שדה מגנטי בכיוון הציר הקל (למיגנוט) נחצות בשדות מגנטיים מתאימים הניתנים לחישוב בסדר ראשון ע"י

$$H_m(n) = \frac{nD}{g\mu_B}.$$

המעבר בין שני המצבים נדון בתחילה ע"י לנדאו וזנר, ויושם במנהור מצבי הספין ב-Fe8. הסתברות המנהור P כאשר סוחפים את השדה האורכי H_z בקצב קבוע באזור בו שתי רמות מצטלבות ניתן ע"י:

$$P = 1\text{-}\exp\left[-\frac{\pi\Delta^2_{m,m'}}{4\hbar g\mu_B\left|m-m'\right|S\,dH/dt}\right]$$

כאשר m ו- m' הם המספרים הקוונטיים של הרמות, dH_z/dt הוא קצב סחיפת השדה ו-$\hbar$ הוא קבוע פלנק.

את התופעה של המינהור הקוונטי ניתן לראות במדידות מקרוסקופיות של המגנטיזציה כפונקציה של השדה . כאשר המערכת נמצאת בשדה מגנטי מתאים H_m (הצטלבות של רמות אנרגיה) יש מעבר של מצבי הספין במינהור וניצן לראות זאת ע"י שינוי חד במגנטיזציה. כאשר הרמות אינן מצטלבות, אין מצבי הספין נשארים קבועים וכן ג ם המגנטיזציה. הדבר מתבטא לבסוף בלולאת היסטרזיס מדורגת , כאשר ב-Fe8 גילו כי מתחת לטמפרטורה של 400 mK הלולאה לא תלויה בטמפרטורה, כלומר מתרחש מנהור "טהור".

ההמילטוניאן הנ"ל אינו יכול להסביר את כל המעברים הנראים בניסוי , ולכן הוצעו מספר אפשרויות של אינטראקציה בין הספין הכולל של המולקולה לסביבה . אחד המודלים מדבר על השפעת השדה הגרעיני על התהליך כולו , ומספר ניסויים הראו קשר בין שינוי השדה הגרעיני (ע"י איזוטופים) ושינוי התנהגות המגנטיזציה (האלקטרונית). כמו כן, חישובים תאורטיים של פיצול המינהור הראו תוצאה הקטנה בשני ס דרי גודל מהערך שנמדד בניסוי.

בעבודה זו אנו מנסים לשנות את השדה הגרעיני וכן את זמני הרלקסציה של הגרעינים ע "י שידור של קרינת רדיו (RF) ולגלות מה ההשפעה על הקפיצות הברורות בעקומת ההיסטרזיס של הגביש , ואולי אף את ההשפעה על פיצול המנהור.

תקציר

המדידות שבוצעו בשיטת מגנטומטר פארדי, הראו בתחילה את האופי הקוונטי של המולקולה כפי שהיה ידוע מניסויים קודמים. מדידות המגנטיזציה בגביש יחיד הראו קפיצות בשדות המתאימים שהשתנו כפונקציה של קצב סחיפת השדה וכפונקציה של הטמפרטורה. לאחר מכן שידרנו פולסים של RF על מנת להעלות את האנרגיה של הגרעינים, ובכל לשנות את השדה שלהם וזמני הרלקסציה. גילינו כי אנו מצליחים לעורר רק כ-10% מגרעיני המימן בדגם, ולאכזבתנו דבר זה לא השפיע על הקפיצות בעקומת ההיסטרסיס.

כתוצר לוואי, גילינו שבכל פעם שיש קפיצה במגנטיזציה, התרמומטר הקרוב לדגם מגיב בעלית הטמפרטורה. לאחר מספר מקרי מבחן הגענו למסקנה שעליית הטמפרטורה נובעת מפליטה של פוטונים מהדגם בשעת המעברים הקוונטים. דבר זה מוכר מהספרות והתגלה גם במגנטים מולקולריים אחרים (Mn12), אך שם זה היה במעברי מפולת (avalanche) בעוד שבניסוי שלנו התופעה התגלתה בכל אחד מהמעברים הקוונטים. עבודות תיאורטיות מרמזות על האפשרות שהתופעה היא סופר-קרינה, שהיא קרינה קוהורנטית שתנאיה נוסחו לראשונה ע"י דיקה ב-1954. בדיקה מראה שתנאי הניסוי עומדים בתנאים לסופר-קרינה.

לסיכום, בניסוי זה הראנו את האופי הקוונטי של המגנט המולקולרי Fe8. הצלחתנו לשנות בצורה חלקית את האינטראקציה בין הגרעינים לאלקטרונים ע"י העלאת הטמפרטורה של כ- 10% מהגרעינים, אך דבר זה לא שינה את עקומת המגנטיזציה של החומר. כמו כן, גילינו שהגביש פולט קרינה אלקטרומגנטית בכל פעם שמתרחש מינהור קוונטי, ובדקנו את התנאים להתרחשותה של סופר-קרינה.